actuators

MDPI

Article

A Realistic Model Reference Computed Torque Control Strategy for Human Lower Limb Exoskeletons

Sk K. Hasan

Department of Mechanical and Manufacturing Engineering, Miami University, Oxford, OH 45056, USA; hasansk@miamioh.edu; Tel.: +1-513-529-0805

Abstract: Exoskeleton robots have become a promising tool in neurorehabilitation, offering effective physical therapy and continuous recovery monitoring. The success of these therapies relies on precise motion control systems. Although computed torque control based on inverse dynamics provides a robust theoretical foundation, its practical application in rehabilitation is limited by its sensitivity to model accuracy, making it less effective when dealing with unpredictable payloads. To overcome these limitations, this study introduces a novel realistic model reference computed torque controller that accounts for parametric uncertainties while optimizing computational efficiency. A dynamic model of a seven-degrees-of-freedom human lower limb exoskeleton is developed, incorporating a realistic joint friction model to accurately reflect the physical behavior of the robot. To reduce computational demands, the control system is split into two loops: a slower loop that predicts joint torque requirements based on reference trajectories and robot dynamics, and a faster PID loop that corrects trajectory tracking errors. Coriolis and centrifugal forces are excluded from the model due to their minimal impact on system dynamics relative to their computational cost. The experimental results show high accuracy in trajectory tracking, and statistical analyses confirm the controller's robustness and effectiveness in handling parametric uncertainties. This approach presents a promising advancement for improving the stability and performance of exoskeleton-based neurorehabilitation.

Keywords: realistic model reference computed torque control; exoskeleton robot; lower extremity dynamic model

check for updates

Citation: Hasan, S.K. A Realistic Model Reference Computed Torque Control Strategy for Human Lower Limb Exoskeletons. *Actuators* **2024**, *13*, 445. https://doi.org/10.3390/act13110445

Academic Editors: Monica Malvezzi, Monica Tiboni and Maria Cristina Valigi

Received: 24 September 2024
Revised: 23 October 2024
Accepted: 4 November 2024
Published: 7 November 2024

Copyright: © 2024 by the author. Licensee MDPI, Basel, Switzerland. This article is an open access article distributed under the terms and conditions of the Creative Commons Attribution (CC BY) license (https://creativecommons.org/licenses/by/4.0/).

1. Introduction

Physical disability significantly impairs a person's mobility and physical capabilities, affecting both individuals and society. Nearly a billion people worldwide face challenges in accessing adequate treatment due to limited resources. Exoskeleton robots offer a promising solution for rehabilitation, providing personalized physiotherapy and continuous performance assessment throughout recovery. This technology holds great potential for enhancing physical therapy and improving neurorehabilitation outcomes for individuals with disabilities affecting both the upper and lower extremities.

Effective rehabilitation with exoskeleton robots requires precise maneuverability, which depends on an integrated control system, combining sensing, actuation, and computation units that communicate via standard protocols and are driven by control algorithms. The high-performance control algorithm execution server functions as the brain of the rehabilitation robot, enabling it to provide passive, active, active-assist, and active-resist therapies. Sensors monitor the robot and facilitate interaction with the user, while actuators, functioning like muscles, move the mechanical components. However, even advanced sensors and actuators are insufficient without efficient control algorithms to ensure proper robot maneuverability. Researchers have developed various linear and nonlinear control algorithms to enhance maneuverability and optimize the delivery of diverse physical therapies.

Table 1 summarizes the features of recent human lower limb exoskeleton robots, detailing their actuated joints, control algorithms, and key characteristics.

Table 1. Overview of existing rehabilitation robots, including their degrees of freedom, sensing, actuation, and control systems.

#	Device Name	Actuated Joints	Control Algorithm	Remarks	Refs.
1.	EXPO and SUBAR	Hip: F-E (A) Knee: F-E (A) Ankle: (U) Double legs	EXPO utilizes a Fuzzy logic controller, while SUBAR is developed with an Impedance controller	The use of the impedance controller in SUBAR offers greater user comfort compared to EXPO	[1,2]
2.	Lokomoat	Pelvis: V.M. (U) Hip: F-E (A) Knee: F-E (A) Ankle: F-E (U) Double legs	Patient-Driven Motion Reinforcement (PDMR) techniques were used to implement the Hybrid Force Position Control System	The PDMR method enables patients to walk at their preferred speed and gait pattern	[3,4]
3.	Lopes	Pelvis: L-R, F-B Hip: F-E(A) A-A (A) Knee: F-E (A) Double legs	An impedance control scheme was implemented	The impedance controller enabled the creation of a virtual therapist action	[5,6]
4.	ALEX	Trunk: 3 DOF Hip: F-E (A), A-A(U) Knee: F-E (A) Ankle: F-E(U) Single leg	A force field controller was implemented, allowing the system to apply appropriate force to follow the desired trajectory	The force field controller enabled the development of the assist-as-needed control technique, which is crucial for active and active-assist types of physical therapy	[7–10]
5.	HAL	Hip: F-E (A) Knee: F-E (A) Ankle: F-E (U) Single leg	HAL single-leg version operates using a hybrid controller that combines Cybernetic Voluntary Control (CVC) and Cybernetic Autonomous Control (CAC). CVC offers physical support based on the user's voluntary muscle activity, while CAC functions using pre-recorded trajectories	CVC is effective when the user has strong voluntary muscle signals, while CAC is more suitable when those signals are weak. This allows the system to accommodate all types of patients	[11–13]
6.	REWALK	Hip: F-E(A) Knee: F-E(A) Foot: F-E(U) Double legs	It operates using pre-recorded trajectories, with a tilt sensor determining the trunk angle to select the most appropriate trajectory for the user's condition	The literature lacks a detailed description of the low-level controller	[14,15]
7.	ELEGS	Hip: A-A (U) F-E (A) Knee: F-E (A) Ankle: F-E (U)	A finite state machine is used to maneuver a series of states.	Different controllers were developed for different states.	[16,17]
8.	Vanderbilt Exoskeleton	Hip: F-E (A) Knee: F-E (A) Double legs	Runs based on preprogrammed trajectories. It has settings for different modes like sitting to stand, walk, stair ascent/descent	The literature lacks a detailed description of the low-level controller	[18]
9.	ATLAS	Hip: F-E (A) Knee: F-E (A) Ankle: F-E(U)	It was developed by integrating a finite state machine with a PD controller, with specific proportional and derivative gains, along with defined entry and exit conditions for each state	The finite state machine, combined with varying gains, functions similarly to a gain scheduling mechanism	[19]

Table 1. *Cont.*

#	Device Name	Actuated Joints	Control Algorithm	Remarks	Refs.
10.	MINA	Hip: F-E (A) Knee: F-E (A) Ankle: F-E(U) Double legs	MINA operates using a PD controller and functions in two phases: the recording phase, where trajectories are collected from healthy subjects, and the running phase, during which the robot follows the pre-recorded trajectories	The use of a PD controller for a type I system is well justified, as it ensures both stability and accuracy	[20]
11.	Mind walker	Hip: A-A (A) F-E(A) Knee: F-E(A) Ankle: F-E (U) Double legs	A joint impedance controller is integrated with a Finite State Machine, where state transitions are triggered by shifts in the center of mass.	This approach is highly effective for controlling walking assistance in lower limb exoskeleton robots. The inclusion of an impedance controller allows the robot to easily match its impedance with the user.	[21]
12.	Walking assistance lower limb exoskeleton	Hip: F-E (A) A-A (U) Knee: F-E (A) Ankle: U Double Legs	The walking assistance robot operates using a finite state machine, with state transitions triggered by the location of the Center of Pressure, determined through data from the inclinometer	The inclinometer mounted on the backbone measures the torso angle.	[22]
13.	IHMC mobility assist exoskeleton	Hip: F-E (A), A-A (A), R-R (U) Knee: F-E (A) Ankle: F-E (U) Double Legs	System operates based on torque and position control, with a PD controller used in both cases.	The PD controller is employed for both position and torque control, with greater emphasis placed on system robustness than on tracking accuracy	[23]
14.	Lower-limb power assist exoskeleton	Hip: F-E(A) Knee: F-E(A) Ankle: U	A PI velocity control loop is placed within a PI torque control loop.	More emphasis was placed on accuracy rather than the robustness of the control system.	[24]
15.	ABLE	Hip: F-E Knee: F-E Ankle: F-E	Powered by a PD controller, the mobile platform, lower limb orthosis, and telescopic crutch operate in synchrony	More focus was given on the stability and disturbance rejection rather than tracking accuracy.	[25]
16.	Nurse robot suit	Supports shoulder, waist, legs	PID control technique	PID control algorithms were employed to achieve a balance between stability and accuracy	[26,27]
17.	BLEEX	Hip: F-E (A), A-A (A), R (U) Knee: F-E (A) Ankle: A-A(U), F-E(A) R	The BLEEX robot operates with a hybrid controller, consisting of two separate controllers: one for the swing phase and another for the stance phase. The swing phase demands high velocity with low torque, while the stance phase requires low velocity with high torque	The combination of the position controller and the positive feedback-based sensitivity controller performed efficiently, resulting in minimal tracking error	[28,29]
18.	CUHK-Exo	Hip: F-E (A), R Knee: F-E (A) Ankle: F-E(P)	At the lower level, a PD controller is utilized, while the upper level employs the Offline Design and Online Modification (ODOM) control technique	Accurately calculating the center of pressure is impractical, but the use of the ODOM adaptation method enhances its functionality	[30,31]
19.	Xor	Hip: F-E (A), R(U) Knee: F-E (A) Ankle: F-E(P), A-A(U)	The system operates on a hybrid driving concept, with pneumatic artificial muscles serving as gravity balancers and an electric motor acting as a compensator	A comparison with the PD controller demonstrates the effectiveness of the proposed controller.	[32]

F-E—Flexion–Extension, A-A—Abduction–Adduction, L-R—Left–Right, F-B—Forward–Backward, A—Actuated, U—Unactuated, VM—Vertical Movement.

Table 1 illustrates that both linear and nonlinear control algorithms are utilized to address nonlinear robot dynamics. Most nonlinear control algorithms rely on a mathematical model of the robot's dynamics, making it essential to create an accurate model as part

of the control architecture. Although the PD and PID techniques do not strictly require a model, having one aids in gain selection and performance evaluation. Developing an accurate robot model is challenging, but feedback control mechanisms offer some protection against modeling inaccuracies. The acceptable modeling error range varies by control technique, with some algorithms being sensitive to errors, while others are more robust against uncertainties [33].

Model-based control utilizes the complete robot model, which includes the mass matrix, gravity vector, and Coriolis and centrifugal forces. The Coriolis and centrifugal forces have a minimal impact on the overall robot dynamics and add high computational cost. Existing studies reveal that there is scope for optimizing computational resources. In the proposed controller, we simplify the model by excluding the Coriolis and centrifugal force terms. To further enhance the controller's robustness against model uncertainties, an additional PID control loop is incorporated. This dual-loop design helps maintain precise trajectory tracking while minimizing sensitivity to inaccuracies in the model and optimizing the controller's computational load. An overall outline of this study is given below.

This study presents a 7-DOF dynamic model of the human lower extremities developed using the Lagrange energy method. To control this model, a novel realistic model reference computed torque controller (RMRCTC) is introduced, providing enhanced protection against discrepancies between the plant and model parameters. Additionally, a realistic friction model is incorporated to simulate the dynamic frictional effects. This study is organized into seven sections. Section 2 covers human lower extremity anatomy, which is crucial for anthropomorphic modeling of the exoskeleton robot. Section 3 describes the development of kinematic and dynamic models and friction modeling. Section 4 details the realistic model reference computed torque control architecture and controller stability analysis. Section 5 presents simulation results along with a discussion, while Section 6 verifies the robustness of the developed controller concerning modeling discrepancies. Section 7 covered the key findings, and the challenges encountered throughout the completion of this project. Finally, Section 8 concludes this research with summary remarks.

2. Human Lower Extremity Anatomy

The human lower extremities are a complex structure, comprising bones, joints, and major muscles that work together to facilitate movement and support the body. The primary bones include the femur (thigh bone), patella (kneecap), tibia (shin bone), and fibula. The hip joint connects the femur to the pelvis and allows for a wide range of motion in multiple planes, providing approximately three degrees of freedom (flexion/extension, abduction/adduction, and internal/external rotation). The knee joint, formed by the femur, tibia, and patella, enables flexion and extension and internal–external rotation, contributing two degrees of freedom. The ankle joint connects the tibia and fibula to the foot, allowing for dorsiflexion and plantarflexion, with additional slight movements of inversion and eversion.

Key muscles include the quadriceps, which extend the knee; the hamstrings, responsible for knee flexion; and the gastrocnemius and soleus muscles in the calf, which facilitate plantarflexion of the foot. The gluteal muscles, including the gluteus maximus, medius, and minimus, play vital roles in hip stabilization and movement. Together, this intricate anatomy supports weight bearing, locomotion, and balance, allowing for efficient and coordinated movement during various activities. Figure 1 shows the human lower extremity degrees of freedoms.

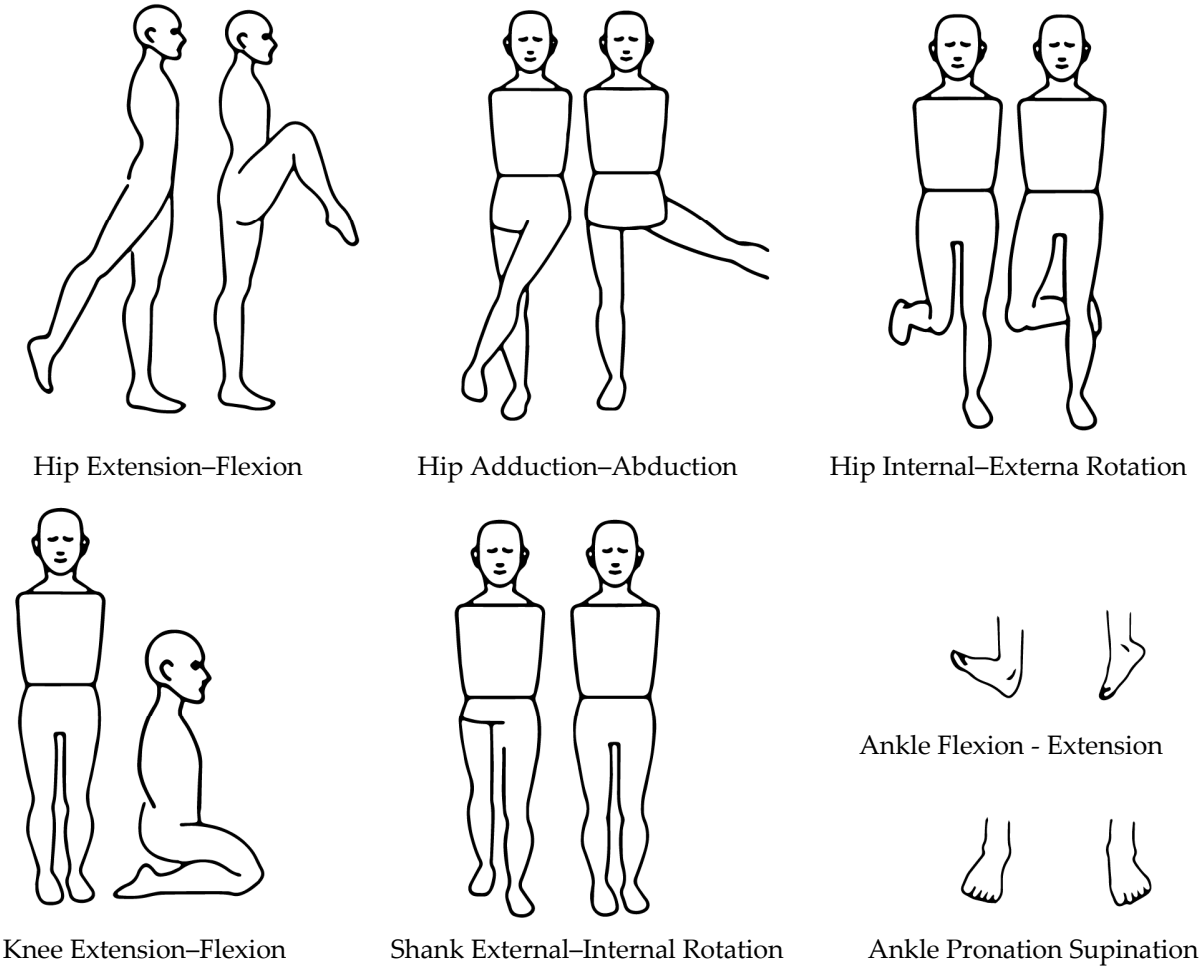


Figure 1. Human lower extremities' degrees of freedom.

2.1. Human Lower Extremity Ranges of Motion

The range of motion in the human lower extremities is essential for determining the joint ranges of motion in exoskeleton robots. Most healthy individuals exhibit similar ranges of motion. However, for physical therapy patients, the acceptable range values differ based on each individual's health condition. Average joint ranges of motion have been documented from various sources [34–36].

The human lower extremities exhibit a wide range of motion across various joints, essential for mobility and functionality. The hip joint allows approximately 120 degrees of flexion, 30 degrees of extension, 45 degrees of abduction, and 30 degrees of adduction, along with internal and external rotation (both are 45 degrees).

The knee joint permits about 135 degrees flexion and limited extension. The ankle joint facilitates dorsiflexion of around 20 degrees and plantarflexion of approximately 50 degrees, along with inversion/pronation and eversion/supination movements (35 degrees and 15 degrees). This extensive range of motion enables activities, such as walking, running, jumping, and climbing, contributing to overall mobility and stability.

2.2. Human Lower Extremity Anthropometric Parameters

Anthropometric properties are essential for developing kinematic and dynamic models of the human lower extremities. Nikolova and Toshev conducted a study analyzing these properties using data from 5290 individuals, including 2435 males and 2855 females, with their findings published in 2008 [37]. Additionally, Contini created empirical equations to determine anthropometric parameters of the human upper and lower extremities based on the subject's weight and height. For this study, we used the empirical formulas

proposed by Contini. Equations (1)–(21) outline the calculations used for determining the anthropometric parameters necessary for dynamic modeling and simulation.

$$B_d = 0.6905 + 0.0297C\frac{lb}{ft^3}, where\ C = HW^{-\frac{1}{3}}, \tag{1}$$

In Equation (1), B_d is the body density (lbs/ft^3), H is the height of the subject $(inch)$, W is the body weight of the subject (lbs). The thigh, shank, and foot densities are determined using Equations (2)–(4),

$$T_d = 1.035 + 0.814 * B_d\frac{lb}{ft^3} \tag{2}$$

$$S_d = 1.065 + B_d\frac{lb}{ft^3} \tag{3}$$

$$F_d = 1.071 + B_d\frac{lb}{ft^3} \tag{4}$$

In Equations (2)–(4), T_d is the thigh density, S_d is the shank density, and F_d is the foot density. The whole-body volume (B_v) was calculated using body weight and body density.

$$B_v = \frac{W}{B_d}ft^3 \tag{5}$$

The volumes of the thigh, shank, and foot were calculated as follows:

$$T_v = 0.0922 * B_v ft^3 \tag{6}$$

$$S_V = 0.0464 * B_v ft^3 \tag{7}$$

$$F_v = 0.0124 * B_v ft^3 \tag{8}$$

The approximate weights of the thigh, shank, and foot were calculated as given using Equations (9)–(11)

$$T_m = T_v * T_d\ lbs \tag{9}$$

$$S_m = S_v * S_d\ lbs \tag{10}$$

$$F_m = F_v * F_d\ lbs \tag{11}$$

The lengths of the thigh (T_l), shank (S_l), foot (F_l) and ankle to lower face of the foot (A_g) were calculated as shown in Equations (12)–(15),

$$T_l = 0.245 * H\ inch, \tag{12}$$

$$S_l = 0.285 * H\ inch, \tag{13}$$

$$F_l = 0.152 * H\ inch, \tag{14}$$

$$A_g = 0.043 * H\ inch \tag{15}$$

The locations of the center of mass from the proximal joint (for thigh (T_{cm}), shank (S_{cm}), foot (F_{cm})) are given by Equations (16)–(18),

$$T_{cm} = 0.41 * T_l\ inch, \tag{16}$$

$$S_{cm} = 0.393 * S_l\ inch, \tag{17}$$

$$F_{cm} = 0.445 * F_l\ inch \tag{18}$$

The empirical equations for the inertial properties of the thigh T_i, shank S_i, and foot F_i are given in Equations (19)–(21),

$$T_i = \begin{bmatrix} T_m(0.124 * T_l)^2 & 0 & 0 \\ 0 & T_m(0.267 * T_l)^2 & 0 \\ 0 & 0 & T_m(0.267 * T_l)^2 \end{bmatrix} \quad (19)$$

$$S_i = \begin{bmatrix} S_m(0.281 * S_l)^2 & 0 & 0 \\ 0 & S_m(0.114 * S_l)^2 & 0 \\ 0 & 0 & S_m(0.275 * S_l)^2 \end{bmatrix} \quad (20)$$

$$F_i = \begin{bmatrix} F_m(0.124 * F_l)^2 & 0 & 0 \\ 0 & F_m(0.245 * F_l)^2 & 0 \\ 0 & 0 & F_m(0.257 * F_l)^2 \end{bmatrix} \quad (21)$$

3. Human Lower Extremity Kinematic and Dynamic Modeling

The human lower extremity exoskeleton robot is designed to be closely attached to the human body, aiming to replicate human joints and movements. The distribution of the moment of inertia in the exoskeleton mirrors that of the human lower limbs. To maintain a general approach rather than focusing on a specific configuration, the anatomical structure and anthropometric parameters of the human lower limbs were used in this simulation. We are actively developing an exoskeleton robot for lower extremity rehabilitation. Figure 2 illustrates the human lower extremity exoskeleton robot currently under development.

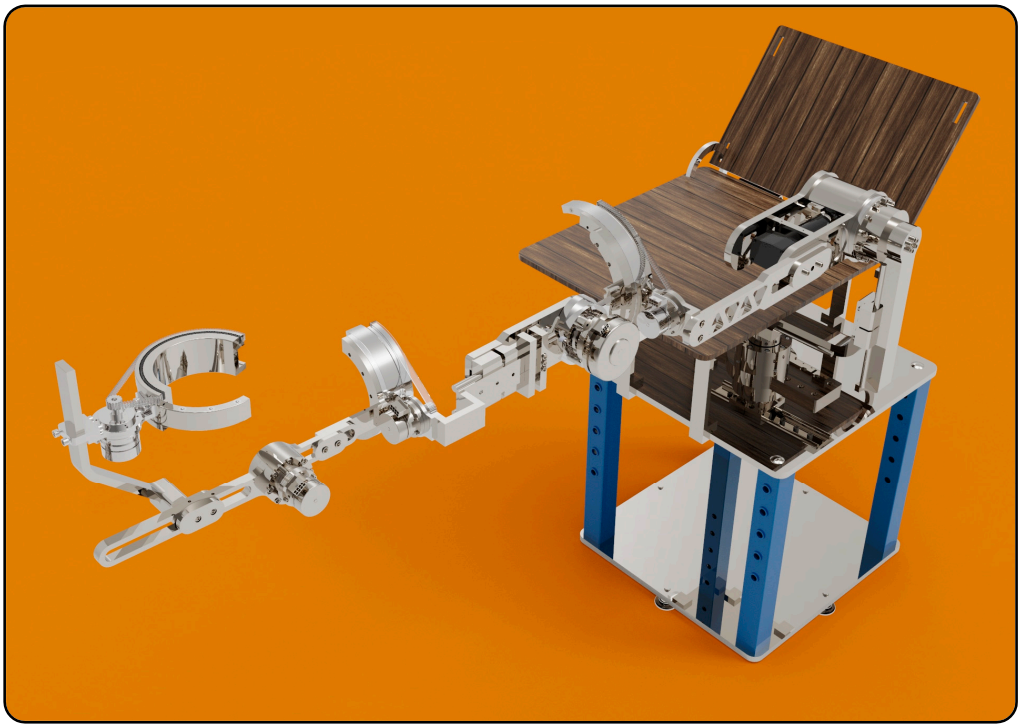


Figure 2. Human lower extremity rehabilitation exoskeleton robot.

3.1. Kinematic and Dynamic Modeling

The kinematic model was developed using the modified Denavit–Hartenberg (DH) parameter method. A separate link frame was assigned to each degree of freedom. Figure 3 illustrates the link frame assignments according to the modified DH parameters. The modified DH parameters for each joint are given in Table 2.

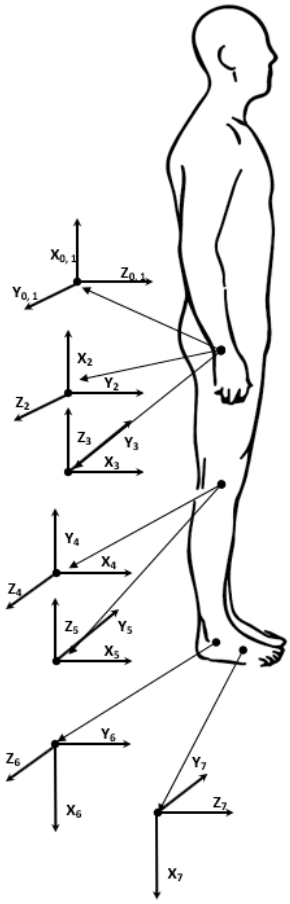


Figure 3. Link frame assignment.

Table 2. Modified DH parameters of human lower extremity.

Gesture Name	Joint Variable	Link Offset	Link Length	Link Twist
	$\boldsymbol{\theta_i}$	$\boldsymbol{d_i}$	$\boldsymbol{a_{i-1}}$	$\boldsymbol{\alpha_{i-1}}$
Hip Abduction/Adduction	q_1	0	0	0
Hip Flexion/Extension	$q_2 - \frac{\pi}{2}$	0	0	$-\frac{\pi}{2}$
Hip Internal/External rotation	q_3	$-l_1$	0	$-\frac{\pi}{2}$
Knee Flexion/Extension	q_4	0	0	$\frac{\pi}{2}$
Knee Internal rotation	q_5	$-l_2$	0	$-\frac{\pi}{2}$
Ankle Dorsiflexion/ Plantarflexion	$q_6 - \frac{\pi}{2}$	0	0	$\frac{\pi}{2}$
Ankle Pronation/Supination	q_7	0	a_1	$-\frac{\pi}{2}$

The general form of the transformation matrix is presented in Equation (22):

$$ {}^{i-1}_{I}T = \begin{bmatrix} \cos\theta_i & -\sin\theta_i & 0 & \alpha_{i-1} \\ \sin\theta_i\cos\alpha_{i-1} & \cos\theta_i\cos\alpha_{i-1} & -\sin\alpha_{i-1} & -\sin\alpha_{i-1}d_i \\ \sin\theta_i\sin\alpha_{i-1} & \cos\theta_i\sin\alpha_{i-1} & \cos\alpha_{i-1} & \cos\alpha_{i-1}d_i \\ 0 & 0 & 0 & 1 \end{bmatrix} \quad (22) $$

By substituting the modified DH parameter values from Table 3 into Equation (22), the resulting transformation matrices, Equations (23)–(29), were obtained.

$$ {}^{0}T_{1} = \begin{bmatrix} \cos(\theta_1) & -\sin(\theta_1) & 0 & 0 \\ \sin(\theta_1) & \cos(\theta_1) & 0 & 0 \\ 0 & 0 & 1 & 0 \\ 0 & 0 & 0 & 1 \end{bmatrix} \tag{23} $$

$$ {}^{1}T_{2} = \begin{bmatrix} \sin(\theta_2) & \cos(\theta_2) & 0 & 0 \\ 0 & 0 & 0 & 0 \\ \cos(\theta_2) & -\sin(\theta_2) & 1 & 0 \\ 0 & 0 & 0 & 1 \end{bmatrix} \tag{24} $$

$$ {}^{2}T_{3} = \begin{bmatrix} \cos(\theta_3) & -\sin(\theta_3) & 0 & 0 \\ 0 & 0 & 0 & -l_1 \\ -\sin(\theta_3) & -\cos(\theta_3) & 1 & 0 \\ 0 & 0 & 0 & 1 \end{bmatrix} \tag{25} $$

$$ {}^{3}T_{4} = \begin{bmatrix} \cos(\theta_4) & -\sin(\theta_4) & 0 & 0 \\ 0 & 0 & -1 & 0 \\ \sin(\theta_4) & \cos(\theta_4) & 0 & 0 \\ 0 & 0 & 0 & 1 \end{bmatrix} \tag{26} $$

$$ {}^{4}T_{5} = \begin{bmatrix} \cos(\theta_5) & -\sin(\theta_5) & 0 & 0 \\ 0 & 0 & 1 & -l_2 \\ -\sin(\theta_5) & -\cos(\theta_5) & 0 & 0 \\ 0 & 0 & 0 & 1 \end{bmatrix} \tag{27} $$

$$ {}^{5}T_{6} = \begin{bmatrix} \sin(\theta_6) & \cos(\theta_6) & 0 & 0 \\ 0 & 0 & -1 & 0 \\ -\cos(\theta_6) & \sin(\theta_6) & 0 & 0 \\ 0 & 0 & 0 & 1 \end{bmatrix} \tag{28} $$

$$ {}^{6}T_{7} = \begin{bmatrix} \cos(\theta_7) & -\sin(\theta_7) & 0 & a_1 \\ 0 & 0 & 1 & 0 \\ -\sin(\theta_7) & -\cos(\theta_7) & 0 & 0 \\ 0 & 0 & 0 & 1 \end{bmatrix} \tag{29} $$

The homogeneous transformation matrix determines the position and orientation of the end frame relative to the base frame. The homogeneous transformation matrix was constructed by multiplying the individual transformation matrices from Equation (23) to Equation (29). For the lower extremities, the homogeneous transformation matrix represents the position and orientation of the foot relative to the hip joint.

$$ {}^{0}_{7}T = \left[{}^{0}_{1}T \; {}^{1}_{2}T \; {}^{2}_{3}T \; {}^{3}_{4}T \; {}^{4}_{5}T \; {}^{5}_{6}T \; {}^{6}_{7}T \right] \tag{30} $$

Lagrange's method is a widely used mathematical approach for deriving dynamic equations of motion. It involves differentiating energy terms with respect to the system variables and time. The dynamic model of the human lower extremities was developed using Lagrange's method [38]. The kinetic energy of a link at any given moment can be calculated using Equation (31).

$$ k_i = \left[\frac{1}{2} m_i . v_{ci}^{T} . v_{ci} + \frac{1}{2} {}^{i}\omega_i^{T} . {}^{ci}I_i . \omega_i \right] \tag{31} $$

In Equation (31), m_i represents the mass of the link, while v_{ci} and ω_{ci} denote the linear and angular velocities of the link at its center of mass. I_i is the moment of inertia of the

link about its center of mass. The total kinetic energy of the model can be calculated using Equation (32).

$$k = \sum_{i=1}^{n} k_i \tag{32}$$

In Equation (32), n represents the total number of degrees of freedom, $n = 7$ for the developed human lower extremity dynamic model.

The potential energy of any link can be calculated using Equation (33),

$$u_i = \left[-m_i . {}^0g^T . {}^0P_{ci} + u_{ref} \right] \tag{33}$$

$$u = \sum_{i=1}^{n} u_i \tag{34}$$

In Equation (33), m_i represents the mass of the link, g is the gravitational acceleration, and ${}^0P_{ci}$ denotes the position of the link's center of mass relative to the ground reference. Finally, by using the Lagrange energy method, the required joint torque can be determined as follows:

$$\tau_i = \left[\frac{d}{dt} \frac{\delta k}{\delta \dot{\theta}_i} - \frac{\delta k}{\delta \theta_i} + \frac{\delta u}{\delta \theta_i} \right] \tag{35}$$

The dynamic equations of motion for the robot are expressed in Equation (36),

$$\tau_{Joint} = \left[M(\theta)\ddot{\theta} + V\left(\theta, \dot{\theta}\right) + G(\theta) \right] \tag{36}$$

In Equation (36), $M(\theta)$ is the mass matrix, a $(7x7)$ symmetric positive definite matrix, $V\left(\theta,\ \dot{\theta}\right)$ is the $(7x1)$ matrix representing the Coriolis and the centripetal terms, and $G(\theta)$ is the $(7x1)$ matrix representing the gravitational term. The τ_{Joint}, $(7x1)$ matrix represents the joint torque requirements. The robot's dynamic equation of motion can be rewritten as follows:

$$\ddot{\theta} = \left[M(\theta)^{-1} \left(\tau_{Joint} - V\left(\theta, \dot{\theta}\right) - G(\theta) \right) \right] \tag{37}$$

Since $M(\theta)$ is a positive definite matrix, $M(\theta)^{-1}$ always exists. Figure 4 shows a schematic diagram of the ideal robot dynamics without counting the joint frictions.

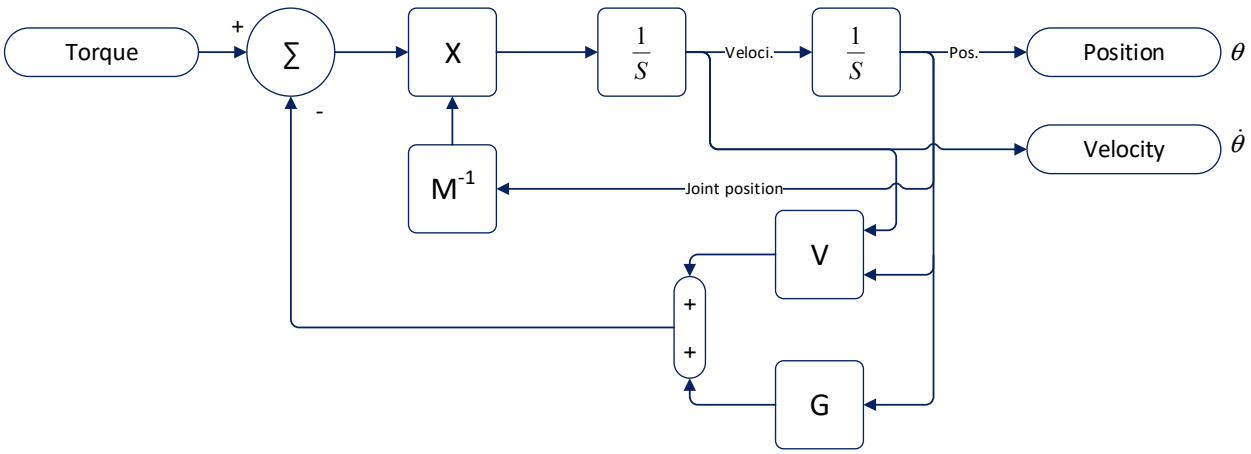


Figure 4. Internal architecture of the robot model.

Friction between two mating parts with relative motion is unavoidable. After considering joint friction torques, the robot dynamical equation becomes,

$$\tau_{Joint} = \left[M(\theta)\ddot{\theta} + V\left(\theta, \dot{\theta}\right) + G(\theta) + \tau_{friction} \right] \tag{38}$$

where

$$\tau_{friction} = \left[F\left(\dot{\theta}\right)\right] \tag{39}$$

Equation (38) can also be written as

$$\ddot{\theta} = \left[M(\theta)^{-1}\left(\tau_{Joint} - V\left(\theta, \dot{\theta}\right) - G(\theta) - F\left(\dot{\theta}\right)\right)\right] \tag{40}$$

Figure 5 presents a schematic diagram of robot dynamics with friction effects.

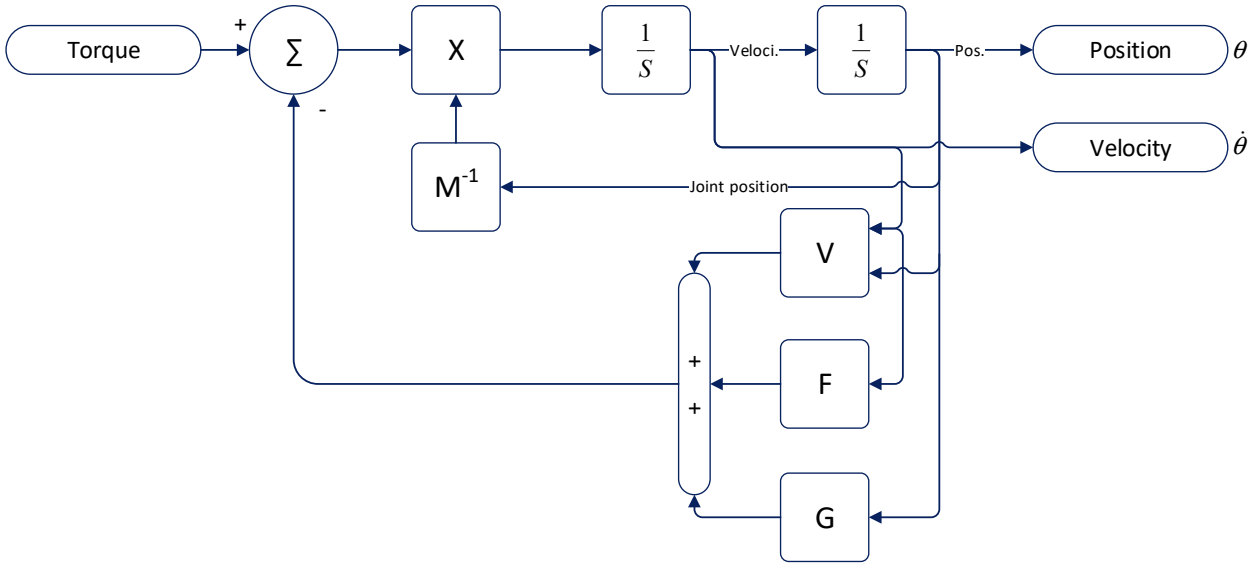


Figure 5. Internal architecture of the physical robot model.

3.2. Friction Modeling

In robotic manipulators, links are connected by bearings, transmissions, or seals, where relative motion at the joints leads to the generation of friction forces. These friction forces can account for as much as 50% of the transmitted force or torque [39]. A robust control system is essential for compensating for the effects of friction. The magnitude of friction force or torque depends on various factors, such as surface roughness, lubricant viscosity, transmitted load, temperature, and the relative velocity between contact surfaces. Since these parameters are variable, it is challenging to develop a comprehensive theoretical friction model.

Most friction models are empirical and have been successfully used for years. Researchers have described friction through models, like the Coulomb friction model, Viscous friction model, Stribeck effect, pre-sliding behavior, stiction phase, and hysteresis effects. Advanced models like the Dahl, LuGre, and Karnopp models [40] also exist. In this study, a friction model combining the Coulomb, Viscous, and Stribeck effects, equivalent to the LuGre model [41], is used. The next section will explain the formulation of the friction model in detail.

Coulomb friction (T_C) is characterized by a constant friction torque, regardless of the velocity or movement of the system, meaning that it remains uniform at any given time. In contrast, **viscous friction** (T_V) produces a resistive torque that is directly proportional to the relative velocity between the surfaces in contact. **Stribeck friction** (T_S) describes a more complex behavior observed at low velocities, where there is a noticeable decrease in friction force, resulting in a negative slope in the friction–velocity relationship. Together, these friction models describe the various types of resistive forces that can occur in mechanical systems.

Equation (41) presents the friction model. Equations (41)–(43) were used to calculate the joint friction torque:

$$T = \sqrt{(2e)}(T_{brk} - T_C).\exp\left(-\left(\frac{\omega}{\omega_{St}}\right)^2\right).\frac{\omega}{\omega_{St}} + T_C.\tanh\left(\frac{\omega}{\omega_{Coul}}\right) + f\omega \quad (41)$$

$$\omega_{St} = \omega_{brk}\sqrt{2} \quad (42)$$

$$\omega_{Coul} = \frac{\omega_{brk}}{10} \quad (43)$$

where

$\boldsymbol{T}$ is the total friction torque.
$\boldsymbol{T_C}$ is the Coulomb friction torque.
$\boldsymbol{T_{brk}}$ is the breakaway friction torque: this is the sum of the Coulomb and Stribeck friction torques near zero velocity, often referred to as breakaway friction.
$\boldsymbol{\omega_{brk}}$ is the breakaway friction velocity, the velocity at which Stribeck friction reaches its peak, and the sum of the Stribeck and Coulomb friction equals the breakaway friction torque.
$\boldsymbol{\omega_{St}}$ is the Stribeck velocity threshold.
$\boldsymbol{\omega_{Coul}}$ is the Coulomb velocity threshold.
$\boldsymbol{\omega}$ is the input angular velocity.
$\boldsymbol{f}$ is the viscous friction coefficient, a proportionality constant between the friction torque and angular velocity, which must have a positive value.

Figures 6 and 7 present the relation between the angular velocity and the generated friction torque.

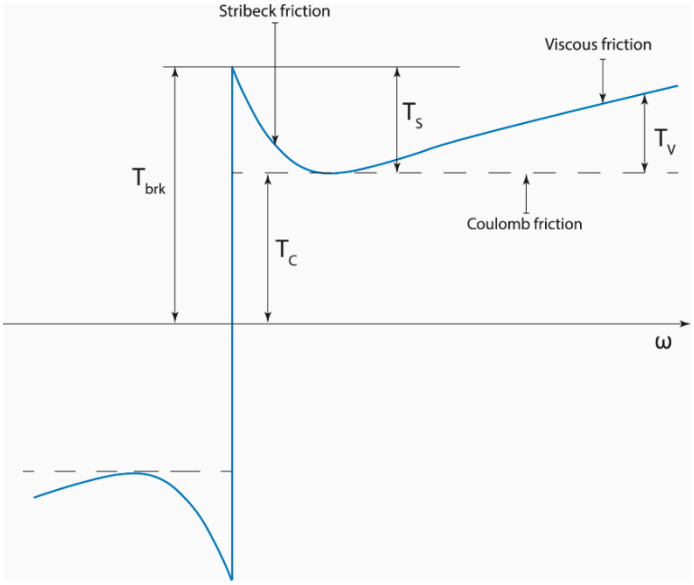


Figure 6. Friction model (combined Coulomb, Viscous and Stribeck effects).

Figure 7 shows the simulated friction torque based on Equations (41)–(43).
In the above simulation, the following assumptions were made:

$$T_{Peak} = 100\ \text{Nm},\ \omega = 100\ \text{rad/s},\ f = 5\ \text{Nm/(rad/s)},\ T_C = 0.1 * T_{Peak}\ \text{Nm},$$
$$\omega_{brk} = 0.01\ \text{rad/s},\ T_{brk} = 0.15 * T_{Peak}\ \text{Nm}$$

Friction between two interacting parts with relative motion is unavoidable. By considering the joint friction torques, the robot's dynamics are modified as follows:

$$\tau_{Joint} = \left[M(\theta)\ddot{\theta} + V\left(\theta, \dot{\theta}\right) + G(\theta) + \tau_{friction}\right] \tag{44}$$

where

$$\tau_{friction} = F\left(\dot{\theta}\right) \tag{45}$$

Equation (38) can be written in the form of Equation (46)

$$\ddot{\theta} = M(\theta)^{-1}\left[\tau - V\left(\theta, \dot{\theta}\right) - G(\theta) - F\left(\dot{\theta}\right)\right] \tag{46}$$

The next section (Section 4) will explain the construction of the realistic model reference computed torque controller (RMRCTC).

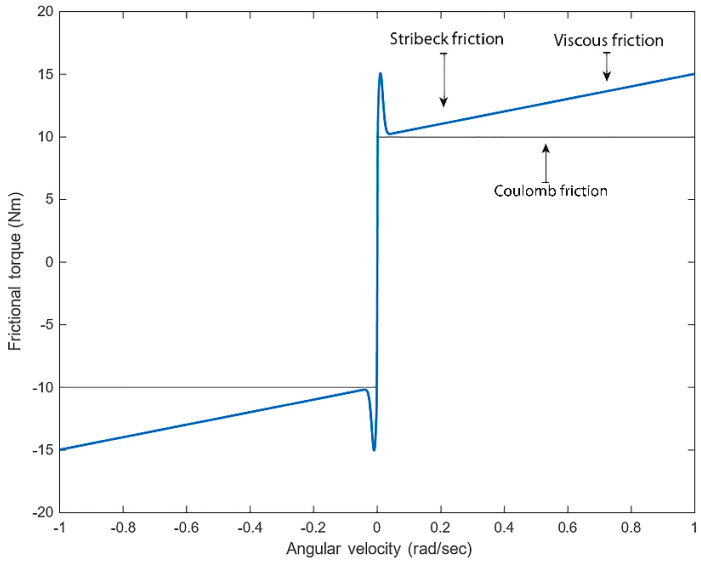


Figure 7. Simulation of the friction model.

4. Realistic Model Reference Computed Torque Control

The realistic model reference computed torque controller is an enhanced version of the standard model reference computed torque controller. One of the key limitations of the traditional model reference computed torque controller is that it requires the dynamic model of the plant to be executed twice during each sampling period, demanding significant computational power [42]. The computed torque control scheme, theoretically based on the plant's inverse dynamics, is utilized within the model reference computed torque controller for real-time torque estimation. The following section will discuss the computed torque controller, the model reference computed torque controller, and the realistic model reference computed torque controller in detail.

4.1. Computed Torque Controller

The computed torque controller is widely recognized as one of the most effective model-based control methods, leveraging inverse dynamics. It consists of two key components: a linearization mechanism and a control action. However, its primary limitation is the need for an accurate dynamic model of the system, making it more suitable for applications such as industrial robotics, where model parameters are well defined. In contrast, rehabilitation exoskeletons must adapt to users with varying body sizes and shapes, making it impractical to accurately measure the mass and inertia of individual limbs. Since the controller's stability and trajectory tracking performance rely heavily on

precise modeling, this presents a significant challenge. Furthermore, the entire dynamic model must be recalculated during each sampling period, placing a heavy computational burden on the control system.

It performs two key functions: first, it linearizes the nonlinear system using feedback linearization, and second, it generates a control input that meets performance criteria [38]. Figure 8 illustrates the architecture of the CTC scheme.

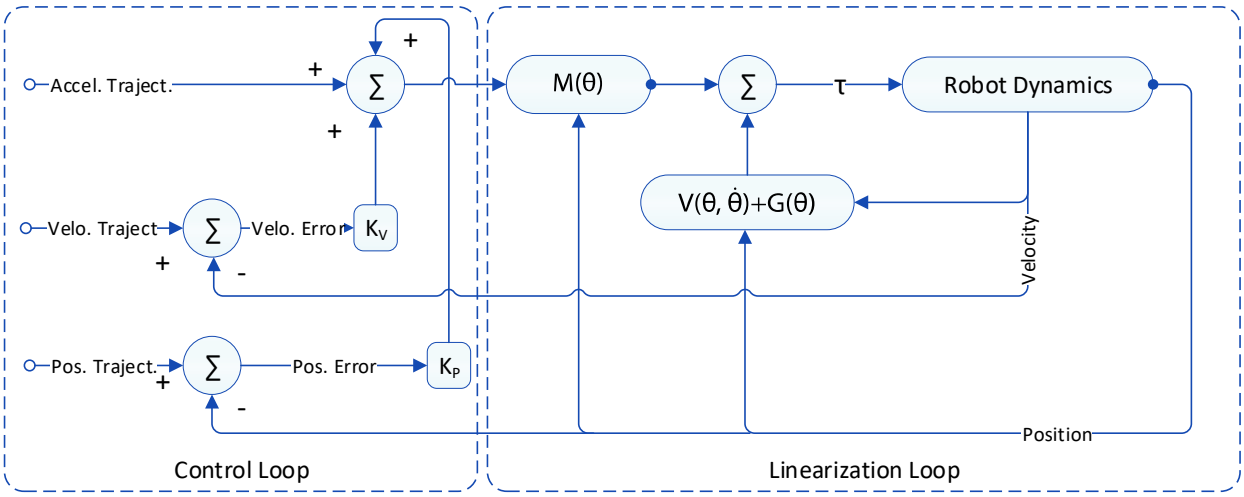


Figure 8. Schematic diagram of the computed torque controller.

In Figure 8, $M(\theta) \in \mathbb{R}^{n \times n}$ represents the robot mass matrix, $V\left(\theta, \dot{\theta}\right) \in \mathbb{R}^{n \times 1}$ indicates the Coriolis and centrifugal forces, and $G(\theta) \in \mathbb{R}^{n \times 1}$ denotes the gravitational force. Figure 8 clearly shows that the CTC relies on the robot's dynamic model for both linearizing the robot dynamics and generating the control input. Consequently, any discrepancies between the robot and its model can result in instability and uncontrolled behavior, making it essential to protect the system from such discrepancies.

4.2. Model Reference Computed Torque Controller

A promising alternative to the computed torque controller is the model reference computed torque controller. In this approach, the plant's model is executed at every sampling time with the help of a computed torque controller for estimating the torque required to track the reference trajectories. The predicted torque is then applied to the physical system. The trajectory tracking error between the model and the physical plant is measured, and any discrepancies are corrected using an additional PID controller. Figure 9 shows a schematic diagram of a model reference computed torque controller. In essence, the model reference computed torque control scheme requires the robot's dynamics to be executed twice in each sampling period (robot's dynamic model and M, G, V matrices). This significantly increases the computational load on the digital controller. A high-speed multiple core digital computer is required to run the control algorithms. The control system consumes a significant amount of energy to run the control algorithms.

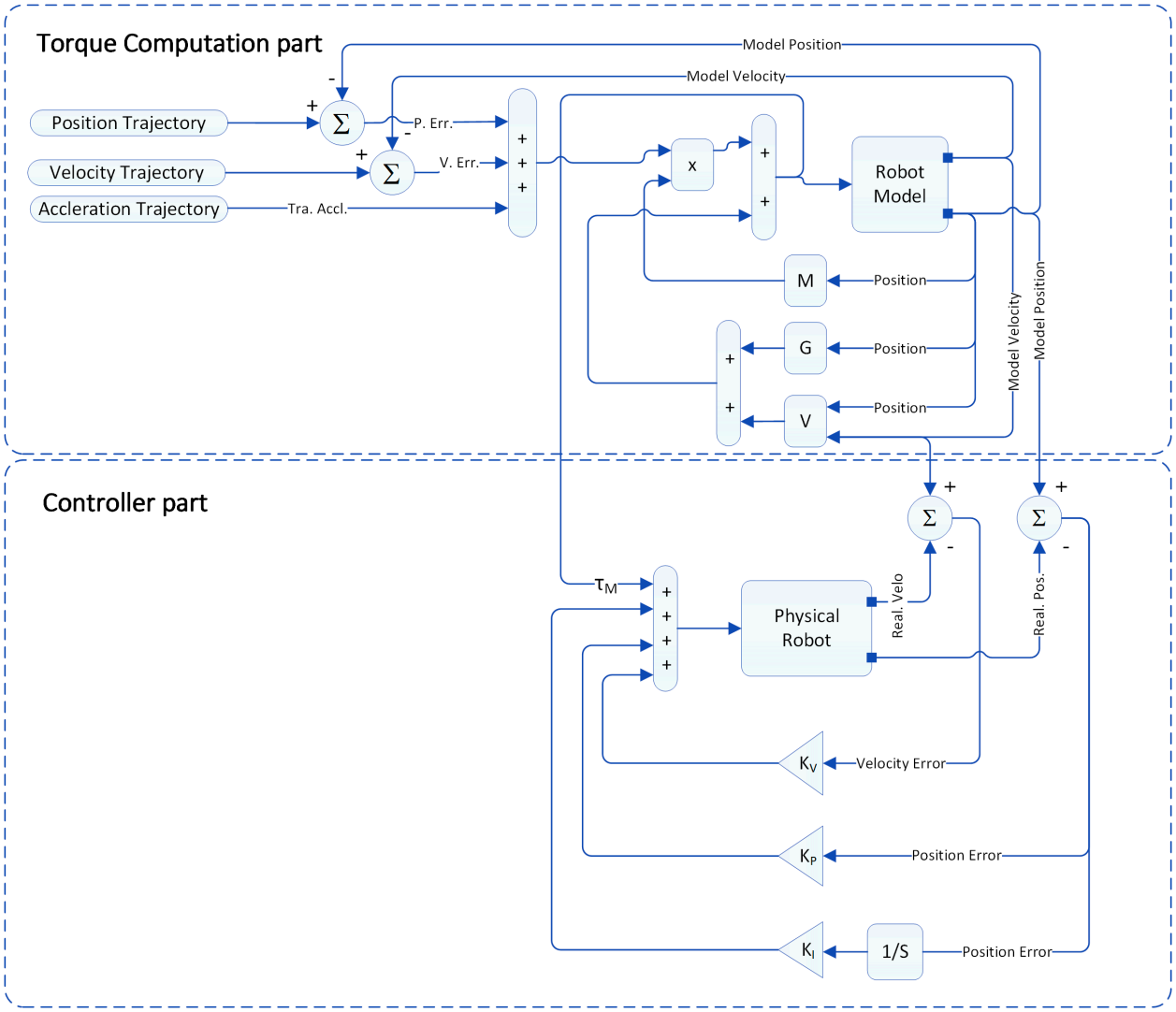


Figure 9. Architecture of model reference computed torque control.

4.3. Realistic Model Reference Computed Torque Controller

In order to make the model reference computed torque controller more efficient and realistic, multiple changes were made in the realistic model reference computed torque controller.

Equation (36) shows that the total torque required to operate the robot is used for accelerating the robot's links and payloads (M matrix), compensating for gravitational effects (G matrix) and counteracting Coriolis and centrifugal effects (V matrix). Often, joint friction is considered as a disturbance. It has been observed that the magnitude of Coriolis and centrifugal forces is significantly smaller compared to the torque needed for acceleration and gravity compensation.

Calculating the Coriolis and centrifugal terms at every sampling period for the robot's specific position and velocity demands more computational power than executing the mass and gravity matrices (M and G matrices).

Figure 10 presents a comparison of the torques needed for three key components: accelerating the links (represented by the mass matrix, M), counteracting gravitational effects (gravity vector, G), and compensating for Coriolis and centrifugal forces (V vector). The results clearly demonstrate that the torque associated with Coriolis and centrifugal forces is significantly smaller than the torque required for accelerating the links or overcoming gravitational forces.

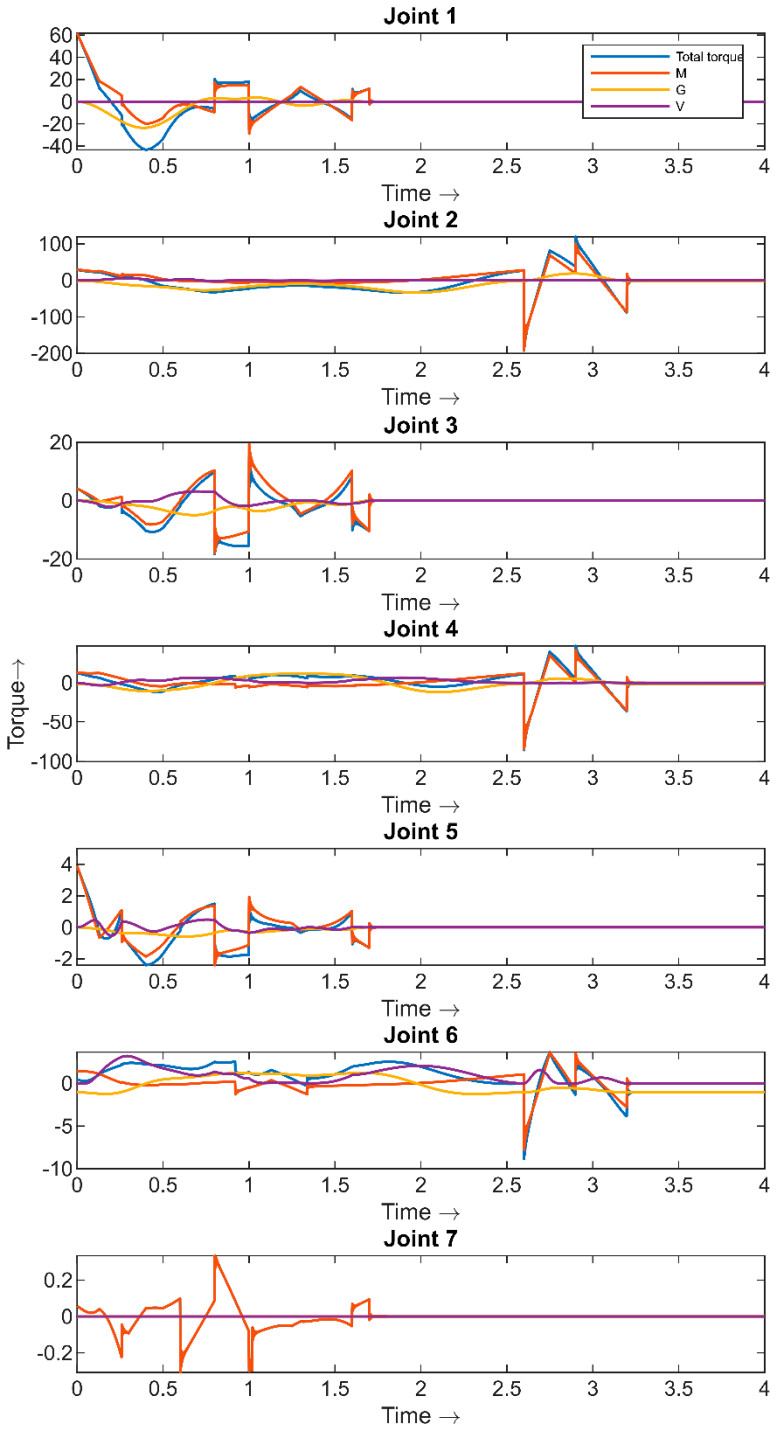


Figure 10. Comparison between the total torque, torque required for link acceleration (M), to overcome the gravity (G), Coriolis and centrifugal forces (V).

To optimize the realistic model reference computed torque controller, we excluded the Coriolis and centrifugal terms from the dynamic model, treating them as disturbances. Additionally, we divided the control algorithm into two loops: slower loop for joint torque estimation and faster loop containing the PID controller for minimizing the tracking error between the reference trajectory and the plant output. The slower loop runs at 100 Hz, while the faster loop runs at 1 kHz. Running two loops at two different rates reduces the computational load and energy consumption for real-time computing. Predicting torque at slower speed causes some inaccuracies. The PID controller was used to remove the errors

and improve the robustness. The developed realistic model reference computed torque controller showed excellent trajectory tracking performance, maintaining small tracking errors, even in the presence of disturbances. By excluding the Coriolis and centrifugal force terms $V\left(\theta,\ \dot{\theta}\right)$, it achieves significantly higher energy efficiency compared to traditional computed torque control and model reference computed torque control methods. Figure 11 shows a schematic diagram of the realistic model reference computed toque controller.

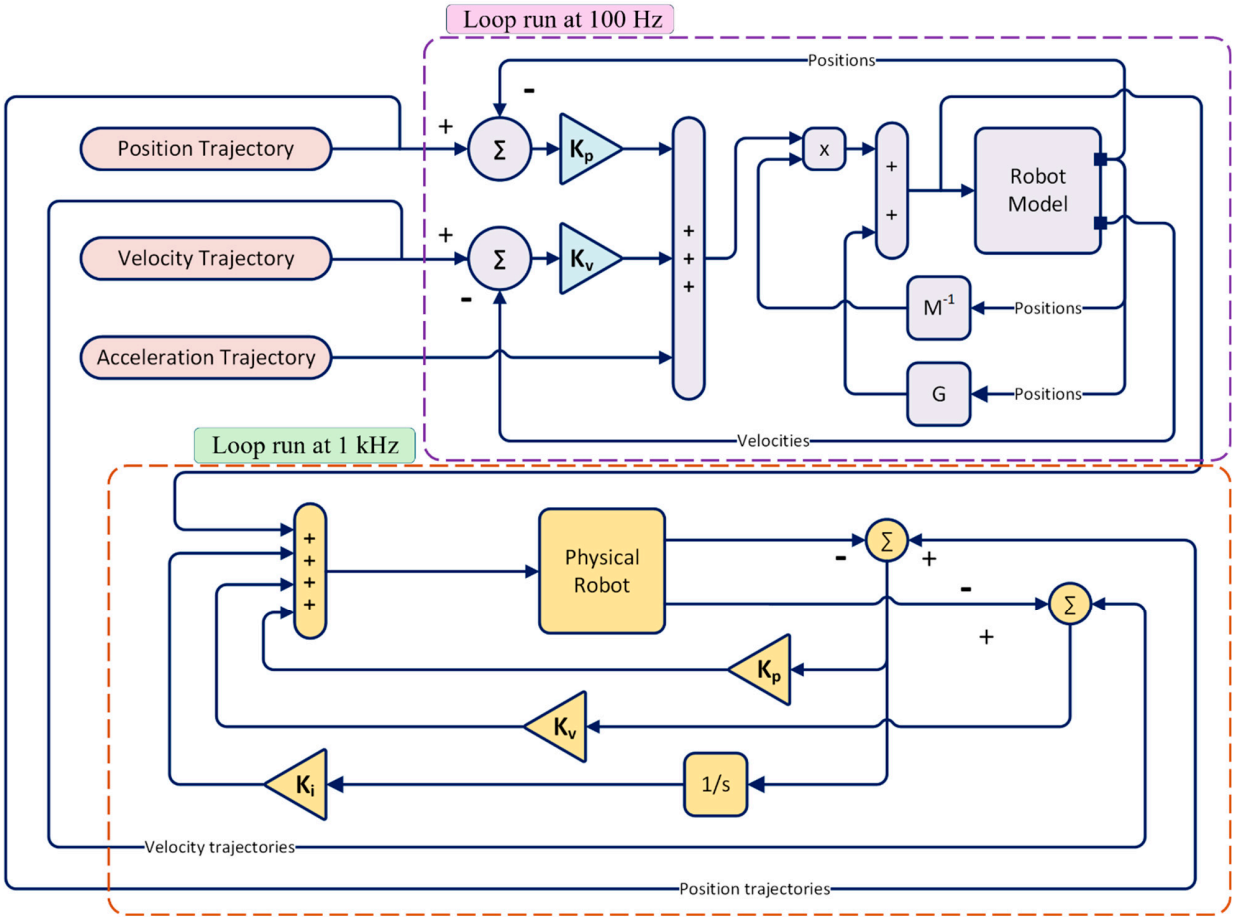


Figure 11. Realistic model reference computed torque control architecture.

Stability Analysis of the Proposed Realistic Model Reference Computed Torque Controller:

Ensuring controller stability is a very fundamental requirement of a control system. The following section will prove the combined system stability by computing the stability of the individual loops.

Loop1:

The dynamic model of the robot can be represented by Equation (47),

$$\left[M(\theta)\ddot{\theta} + V\left(\theta,\dot{\theta}\right) + G(\theta)\right] = \tau_{Joint} \tag{47}$$

The control torque for the model is calculated by using Equation (48),

$$\tau_M = M(\theta)\left[\ddot{\theta}_d + K_v\left(\dot{\theta}_d - \dot{\theta}\right) + K_P(\theta_d - \theta)\right] \tag{48}$$

By comparing Equations (47) and (48),

$$\left(\ddot{\theta}_d - \ddot{\theta}\right) + K_V\left(\dot{\theta}_d - \dot{\theta}\right) + K_P(\theta_d - \theta) = 0 \tag{49}$$

The robot tracking error is defined as $E = (\theta_d - \theta)$. Using Equation (49), the error dynamics can be expressed as follows:

$$\ddot{E} + K_V \dot{E} + K_P E = 0 \tag{50}$$

By applying the Laplace transform in Equation (50), the closed-loop characteristic polynomial can be written as

$$\Delta_C(S) = \left| S^2 I + K_V S + K_P \right| \tag{51}$$

where

$$K_P = diag\{K_{Pi}\} \tag{52}$$

$$K_V = diag\{K_{Vi}\} \tag{53}$$

According to the Routh Hurwitz stability criteria in Table 3, Equation (51) is asymptotically stable as long as the gain matrices $(K_P,\ K_V)$ are positive and definite.

Table 3. Routh Hurtz stability criteria.

S^2	1	K_P
S^1	K_V	0
S^0	K_P	

Loop 2:

This calculates the deviation of the plant output from the model $(e,\ \dot{e})$ and forces the plant to compensate for the tracking errors in a controlled way. Based on the developed RMRCTC scheme, the plant input torque (τ_P) can be calculated as

$$\tau_P = \tau_M + K_I \int (\theta_M - \theta_P) + K_P(\theta_M - \theta_P) + K_V\left(\dot{\theta_M} - \dot{\theta_P}\right) + \tau_f \tag{54}$$

In developing this controller, it is assumed that the model and the plant share the same dynamical structure, differing only in their parameters.

The tracking error $\left(E,\ \dot{E}\right)$ between the model and the plant is defined as

$$E = (\theta_M - \theta_P) \tag{55}$$

$$\dot{E} = \left(\dot{\theta}_M - \dot{\theta}_P\right) \tag{56}$$

$$\tau_P = \tau_M + K_V \dot{E} + K_I \int E + K_P E + \tau_f \tag{57}$$

$$\tau_P(S) = \tau_M(S) + \frac{K_I E(S)}{S} + K_P E(S) + K_V S E(S) + \tau_f(S) \tag{58}$$

$$\tau_P(S) - \tau_M(S) - \tau_f(S) = \frac{\left(S^2 K_V + S K_P + K_I\right) E(S)}{S} \tag{59}$$

Using Equation (59), the error dynamics can be expressed as follows:

$$\frac{E(S)}{\tau_P(S) - \tau_M(S) - \tau_f(S)} = \frac{S}{S^2 K_V + S K_P + K_I} \tag{60}$$

Equation (60) represents the transfer function of the tracking error

Table 4 shows that the control system will be asymptotically stable if the gain matrices $K_P,\ K_V,\ K_I$ are positive and definite. Here, $K_P,\ K_I,\ K_V$ are the $(7x7)$ diagonal matrices.

$$K_P = diag\{K_P\} \tag{61}$$

$$K_I = diag\{K_I\} \tag{62}$$

$$K_V = diag\{K_V\} \tag{63}$$

Table 4. Routh Hurwitz stability criteria for the error dynamics.

S^2	K_V	K_I
S^1	K_P	0
S^0	K_I	

An analysis of the stability of Loop 1 and Loop 2 quickly leads to the conclusion that the proposed control system is asymptotically stable as long as the gain matrices are positive and definite.

5. Simulation Results and Discussion

The trajectory tracking simulation was conducted in a MATLAB-Simulink® environment. The mass and inertial properties of the human lower extremities used in the simulation are listed in Table 5. Controller gains for both the computed torque control (Loop 1) and the PID controller (Loop 2) are also provided in Table 5. The simulation was performed for both sequential and simultaneous joint movements. Figures 12–19 display the results of the developed controller for the human lower extremity's sequential and simultaneous joint movements.

Table 5. Simulation parameters for the HLE dynamic control using MRCTC.

Subject mass		Distance between proximal joint and the center of mass	Thigh	6.69 in (170 cm)		
			Shank	7.48 in (18.92 cm)		
			Foot	4.5 in (11.5 cm)		
Subject mass	163 lb. (73.95 kg)	Thigh inertia g·cm^2 (kg·m^2)		$151 * 10^3$ (0.0151)	0	0
				0	$700 * 10^3$ (0.070)	0
Subject height	67 in (170.18 cm)			0	0	$700 * 10^3$ (0.070)
Thigh Mass	12.45 lb. (5.65 kg)	Shank inertia g·cm^2 (kg·m^2)		$648 * 10^3$ (0.06480)	0	0
				0	$107 * 10^3$ (0.0107)	0
Shank mass	7.67 lb. (3.48 kg)			0	0	$620 * 10^3$ (0.0620)
Foot Mass	2.05 lb. (0.93 kg)	Foot inertia g·cm^2(kg·m^2)		$10 * 10^3$ (0.001)	0	0
				0	$37 * 10^3$ (0.0037)	0
Thigh-length	16.14 in (41 cm)			0	0	$41 * 10^3$ (0.0041)
Shank length	18.89 in (48.79 cm)	**PD controller gains Loop 1**			**PID controller gains Loop 2**	
		K_P		[500, 500, 500, 500, 500, 500, 500]	K_P	[10^4, 10^4, 10^4, 10^4, 10^4, 10^4, 10^4]
Foot length	10.23 in (25.88 cm)	K_V		[7.5 × 10^3, 7.5 × 10^3, 7.5 × 10^3, 7.5 × 10^3, 7.5 × 10^3, 7.5 × 10^3, 7.5 × 10^3]	K_I	[250, 250, 250, 250, 250, 250, 250]
					K_V	[55 × 10^3, 50 × 10^3, 55 × 10^2, 3 × 10^2, 55 × 10^2, 55 × 10^2, 55 × 10^2]

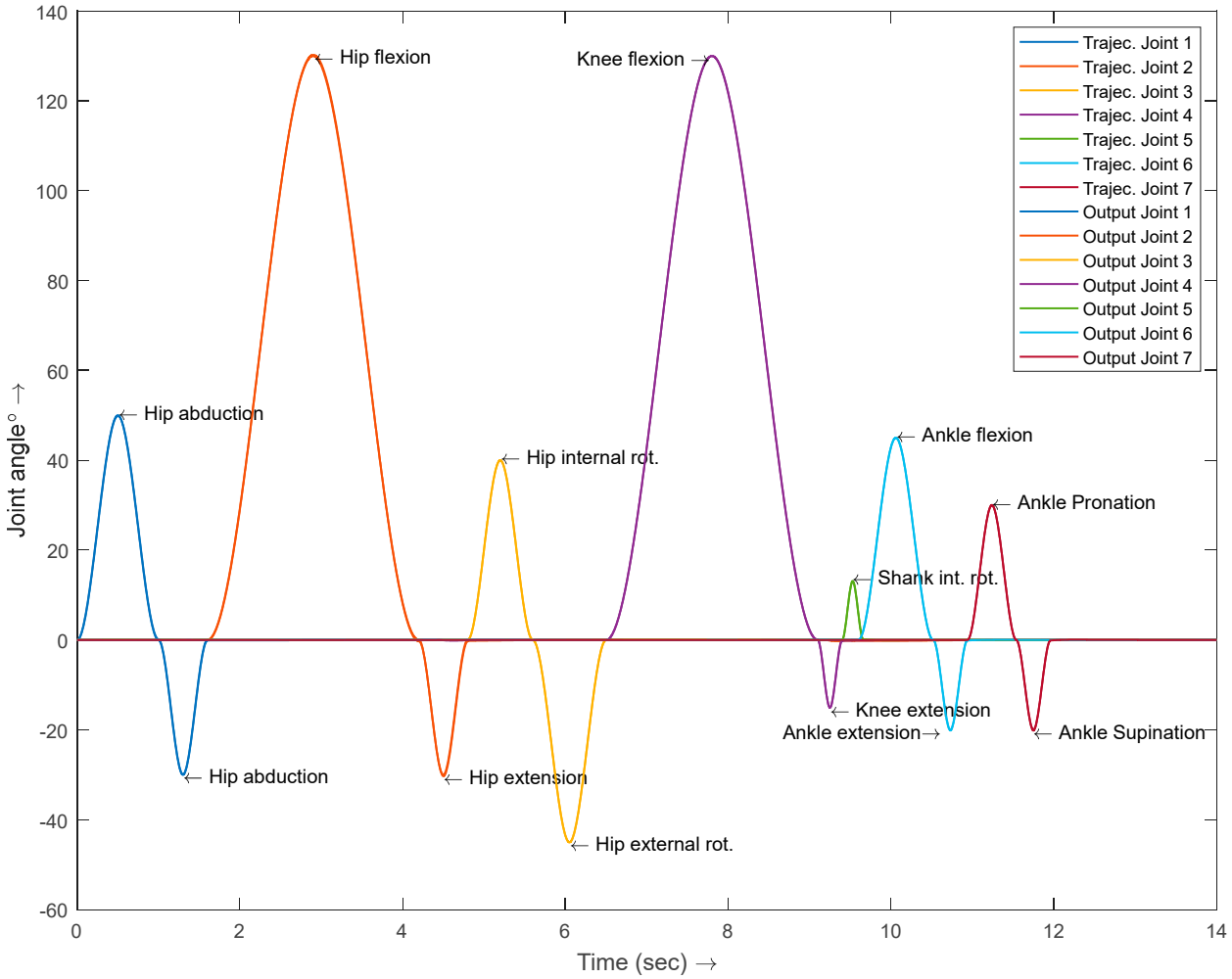


Figure 12. Simulation result using MRCTC for sequential joint movement.

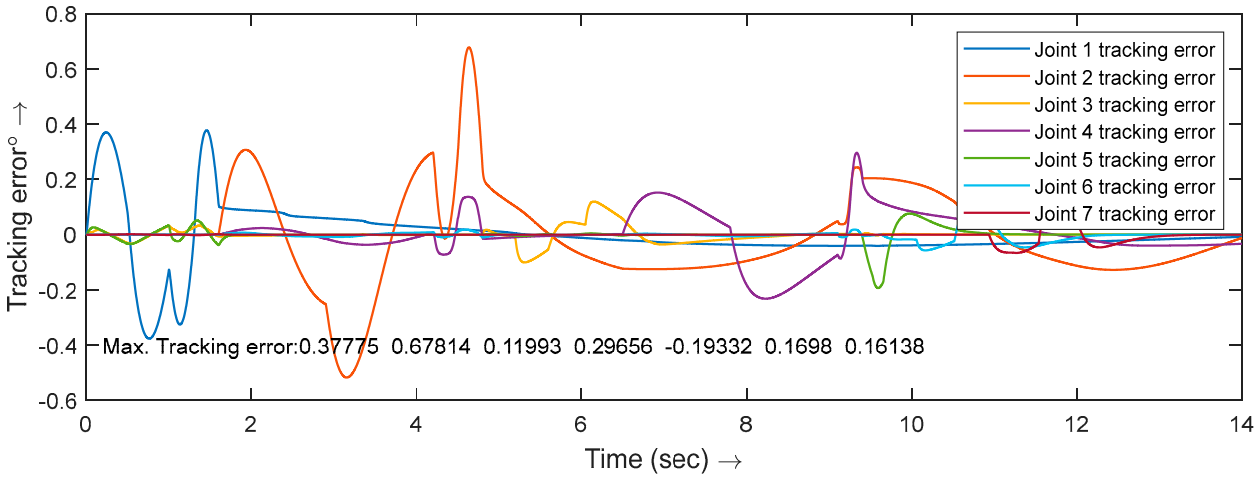


Figure 13. Tracking error using MRCTC for sequential joint movement.

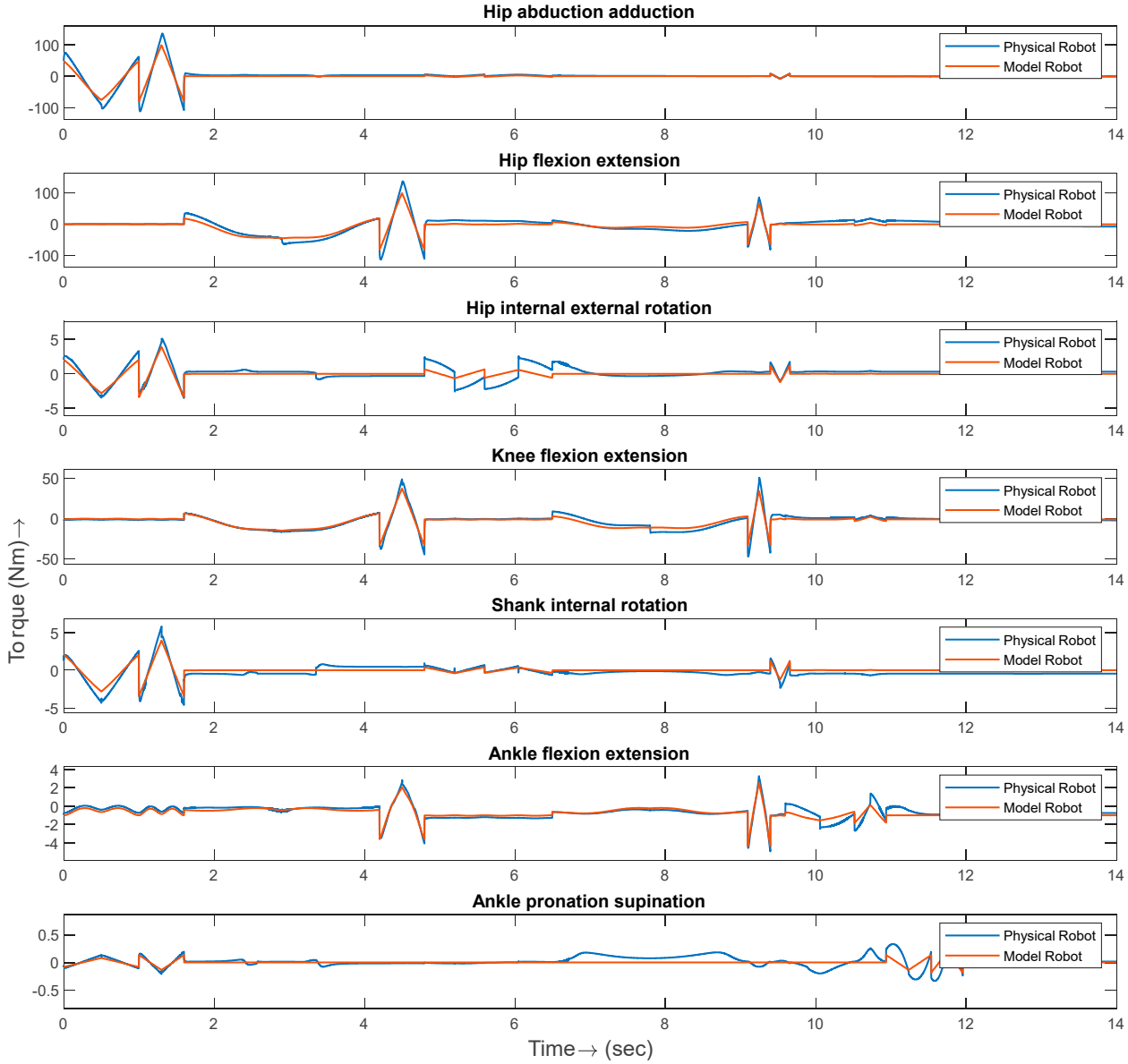


Figure 14. Joint torque required during sequential joint movement using MRCTC.

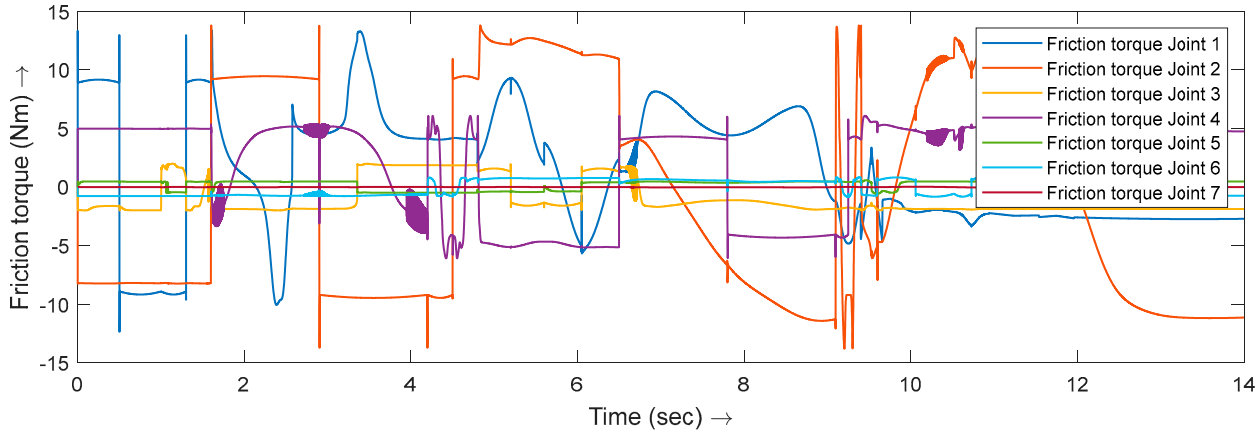


Figure 15. Joint friction torque required during sequential joint movement.

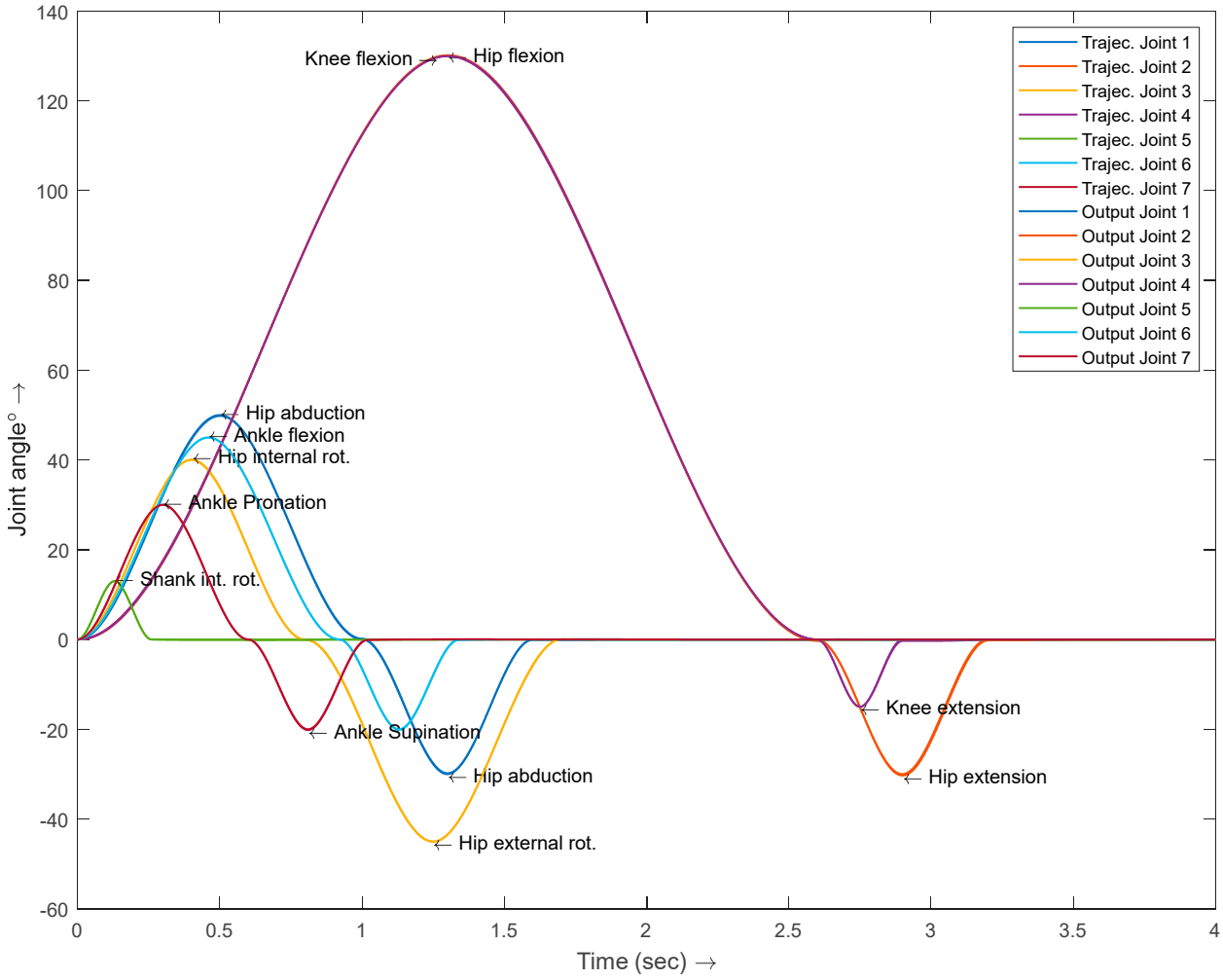


Figure 16. Simulation result for simultaneous joint movement using MRCTC.

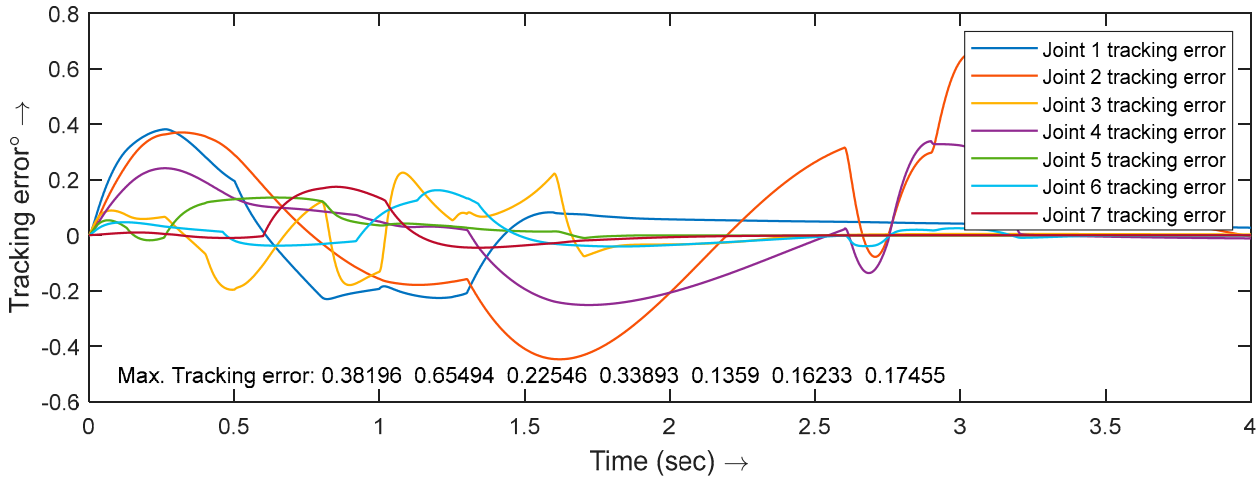


Figure 17. Tracking error during simultaneous joint movement using MRCTC.

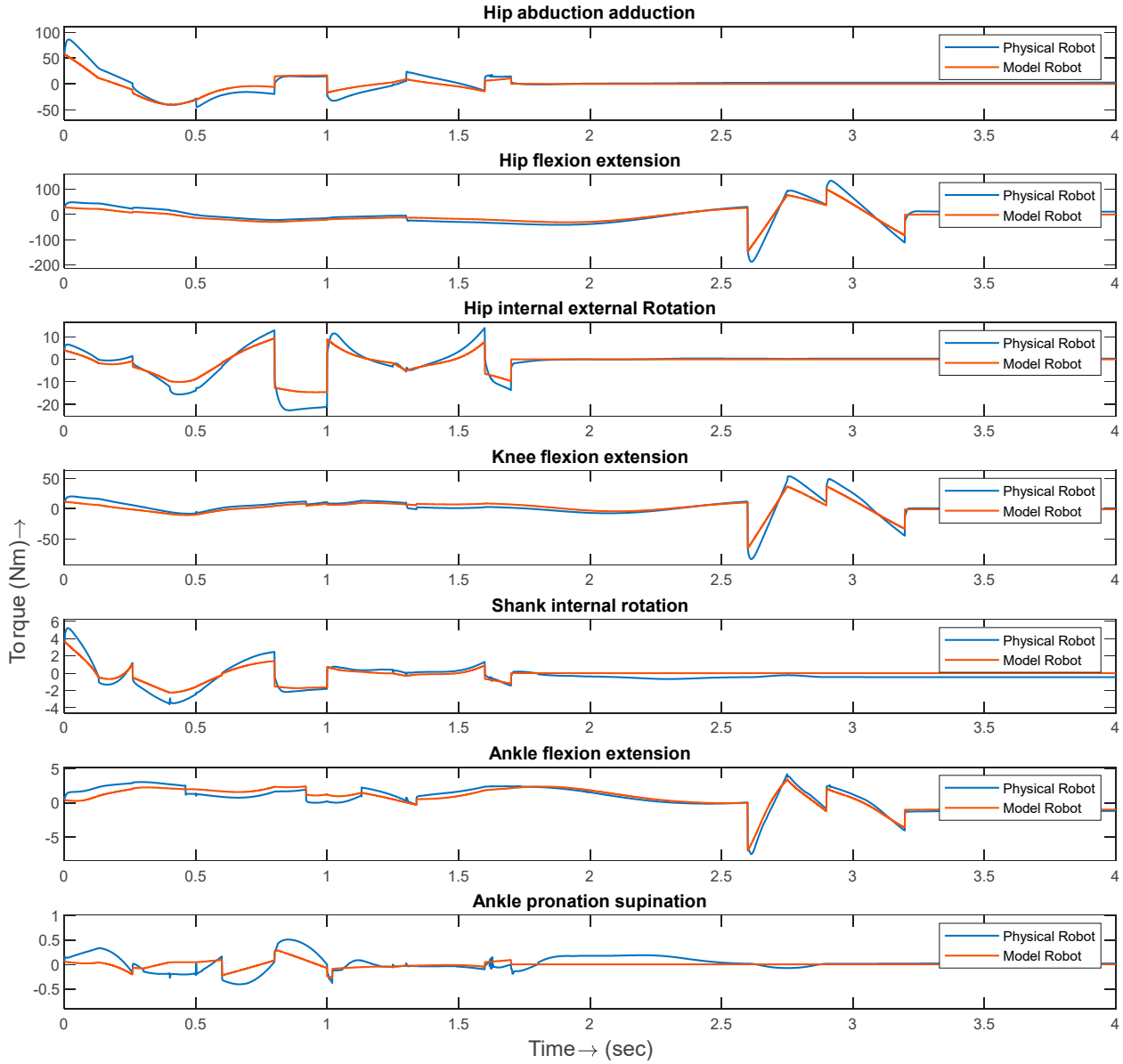


Figure 18. Joint torque requirements for the model and physical robot during simultaneous joint movement with RMRCTC.

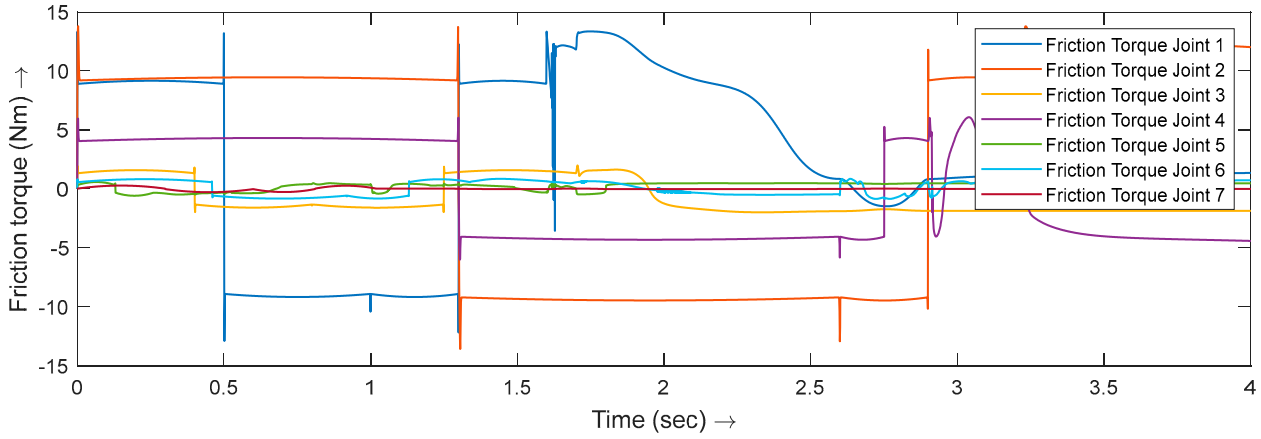


Figure 19. Friction torque during simultaneous joint movement.

The parameters used for modeling dynamic friction are listed below:

$$f = 0.1\ \text{Nm}/(\text{rad}/\text{s}),\ \tau_{coulomb} = 0.1 * \tau_{peak}\ \text{Nm},\ \tau_{brake} = 0.15 * \tau_{peak}\ \text{Nm},$$
$$\omega_{stribeck} = \sqrt{2}\omega_{brake}\ \text{rad}/\text{s},\ \omega_{coulomb} = 0.10 * \omega_{brake}\ \text{rad}/\text{s}$$

The peak torques were calculated based on the torque required to track the same trajectory using the dynamic model of the human lower extremities.

Figures 12–15 illustrate the tracking performance, including trajectory tracking, tracking error, joint torque, and friction torque generated during sequential joint movement.

Figure 12 shows the input trajectory (Trajec. Joint #) supplied to the robot and the resultant output (Output Joint #) trajectories. The simulation result indicates that the output closely follows the input trajectories with minimal error. Figure 13 provides a more detailed view of the tracking errors.

Figure 13 shows that the maximum tracking errors for the sequential joint movements hip abduction–adduction, hip flexion–extension, hip internal–external rotation, knee flexion–extension, shank internal rotation, and ankle flexion–extension and pronation–supination were [0.38°, 0.68°, 0.12°, 0.29°, −0.19°, 0.17°, 0.16°], respectively.

Figure 14 shows the joint torque needed for the model (orange color) and the physical robot joints (blue) during the tracking of sequential joint movements. It is observed that the plant requires more torque than the model. The torque required by the plant consists of two components: firstly, the torque necessary for the model for tracking the trajectory and, secondly, the additional torque required for compensating the differences between the plant input trajectory and the plant's output.

Figure 15 presents the frictional torque generated in the joints during sequential joint movements. Equation (41) was used for estimating the dynamic friction torque generated in the joints due to relative motion between the mating surfaces. The simulation results indicate that joint 2 experienced the highest friction, followed by joints 1 and 4. In comparison, joints 3, 5, 6, and 7 produced significantly lower friction torque than joints 1, 2, and 4.

Figures 16–19 present the tracking performance of the RMRCTC during simultaneous joint movements. Figure 16 shows the input (Trajec. Joint #) and output (Output Joint #) trajectories, demonstrating that the output trajectories closely followed the input trajectories.

Figure 17 illustrates the tracking errors that occurred during simultaneous joint movements, with all joints starting simultaneously and tracking the input trajectories. The maximum tracking errors recorded were [0.38°, 0.65°, 0.22°, 0.33°, 0.13°, 0.16°, 0.17°].

Figure 18 illustrates the joint torque required by both the model and the plant during simultaneous joint movements. Similar to sequential joint movements, the plant required more torque than the model for simultaneous movements.

The torque required by the plant consists of the torque needed by the model, along with additional torque to compensate for the relative errors between the input trajectory and the plant's output.

Figure 19 shows the friction torque generated during simultaneous joint movements. Similar to the sequential joint movements, joint 2 experienced the highest friction torque, followed by joints 1, 4, and the others.

All the PID controller gains used to make the plant behave like the model were determined through trial and error. Fine-tuning the controller gains may further reduce the tracking error.

Figure 19 shows the joint friction torque developed during the simultaneous joint movements.

6. Controller Performance Verification

Statistical analysis was conducted to assess the controller's robustness and tracking performance under extreme conditions. Of the dynamic model's various parameters, only two were variable: the subject's weight and height. These two parameters were adjusted (as shown in Table 6), and different values were applied while collecting the resulting trajectory tracking errors.

Table 6. Weight and height used for statistical analysis.

Subject's Weight	Subject's Height
150 lbs.	50 inches
160 lbs.	55 inches
170 lbs.	60 inches
180 lbs.	65 inches
190 lbs.	70 inches
200 lbs.	75 inches

Figure 20 illustrates the joint trajectory tracking errors for the various weights and heights of the subject. The error histogram reveals that changes in the subject's weight have a negligible impact on the trajectory tracking errors, while variations in height do affect them. The median and standard deviation of the joint trajectory tracking errors were also calculated, and the maximum possible trajectory tracking errors are tabulated in Table 7.

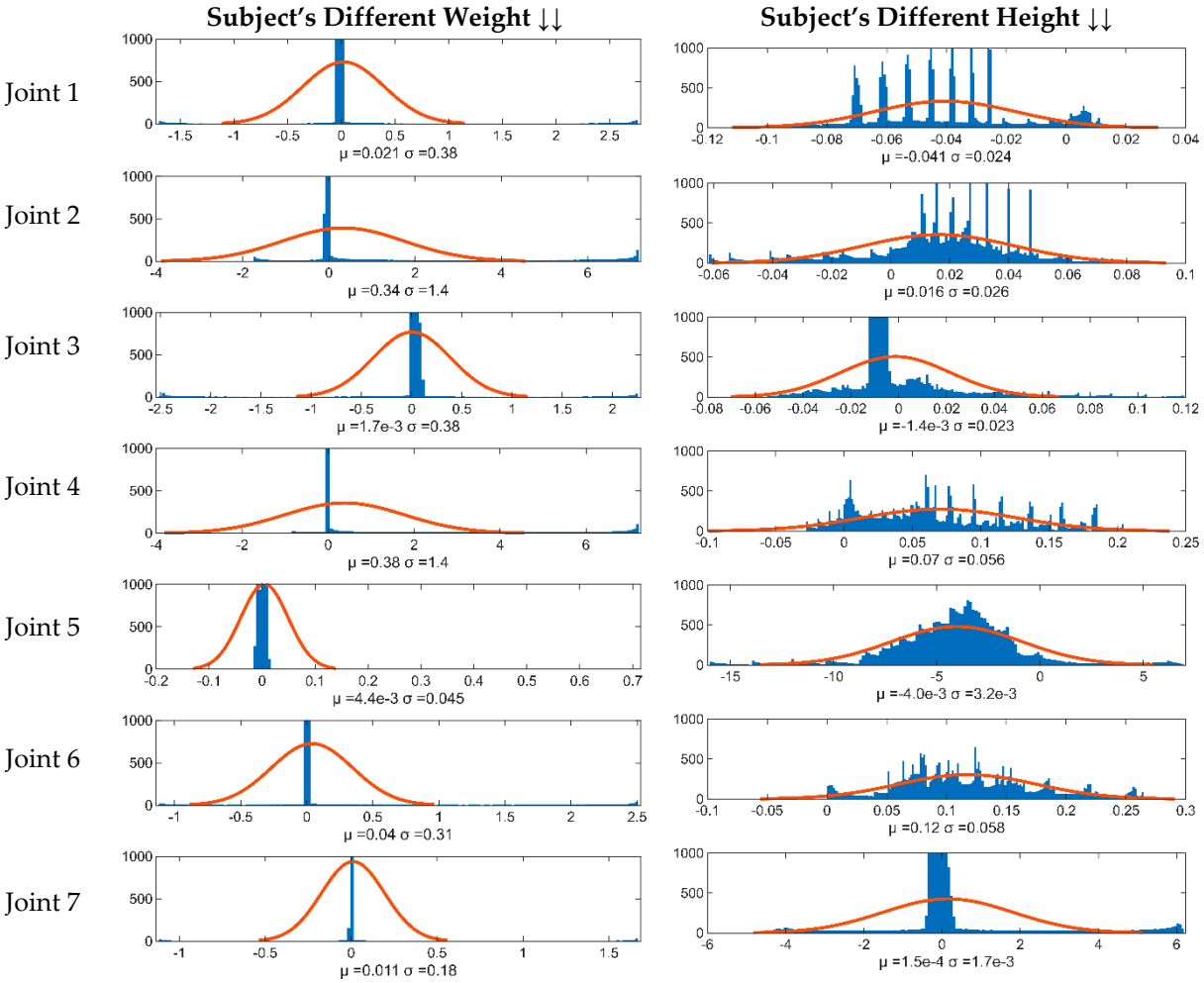


Figure 20. Joint tracking error histogram based on subject's weight and height variations.

Based on the obtained mean/median and the standard deviation, the maximum possible trajectory tracking errors were calculated. Syms like joint 2 and joint 5 have higher standard deviation that may lead to tracking errors up to 5°. It can also be concluded that, based on the subject's height and weight, the controller's gain can be tuned to obtain better accuracy.

Table 7. Mean and variance of the trajectory tracking errors.

Trajectory Tracking Error	Weight		Max Error (99.70% Coverage)	Height		Max Error (99.70% Coverage)
	Median (μ)	STD (σ)	($\mu \pm 3\sigma$)	Median (μ)	STD (σ)	($\mu \pm 3\sigma$)
Joint 1	0.021	0.38	1.16	-0.041	0.024	0.113
Joint 2	0.34	1.4	4.54	0.016	0.026	0.094
Joint 3	1.7×10^{-3}	0.38	1.14	-1.4×10^{-3}	0.023	0.070
Joint 4	0.38	1.4	4.58	0.07	0.056	0.238
Joint 5	4.4×10^{-3}	0.045	0.13	-4×10^{-3}	0.023	0.073
Joint 6	0.04	0.31	0.97	0.07	0.056	0.238
Joint 7	0.011	0.18	0.55	-4.0×10^{-3}	3.2×10^{-3}	0.0136

7. Discussion

This study demonstrates a significant advancement in the control of exoskeleton robots for neurorehabilitation. It addresses the critical challenges associated with traditional computed torque control systems. Inverse dynamics-based computed torque control offers a solid theoretical framework, but its reliance on highly accurate models restricts its practical application in rehabilitation scenarios, particularly when unpredictable payloads or parametric uncertainties are present. To overcome these obstacles, this research introduces a novel realistic model reference computed torque controller that balances the accuracy and computational efficiency.

One of the key contributions of this study is the development of a dynamic model of a seven-degrees-of-freedom (7-DOF) human lower limb exoskeleton, which integrates a realistic joint friction model. This model better reflects the exoskeleton's physical behavior, addressing a limitation often overlooked in traditional controllers. Additionally, the exclusion of Coriolis and centrifugal forces from the model is a noteworthy design choice. While these forces are essential in some dynamic systems, their limited impact on the performance of exoskeleton robots justifies the decision to reduce the computational complexity. This highlights the importance of selectively balancing accuracy and computational efficiency in rehabilitation robotics.

The innovative two-loop control strategy introduced in this research is particularly promising. By separating the control system into a slower predictive loop, responsible for estimating joint torque demands, and a faster PID loop, which quickly corrects trajectory tracking errors, this design ensures both accurate motion control and responsiveness. This dual-loop approach addresses the trade-off between computational efficiency and real-time control, which is critical in exoskeleton-based therapy, where precise motion tracking and responsiveness are essential for patient safety and therapeutic effectiveness.

The experimental validation of the proposed controller demonstrates its robustness and reliability in handling parametric uncertainties. High accuracy in trajectory tracking, combined with statistical evidence supporting the controller's stability, suggests that this approach can significantly enhance the performance of exoskeleton robots. The ability to accommodate model inaccuracies and unpredictable payloads makes the proposed controller highly suitable for real-world neurorehabilitation settings, where patient movements can vary unpredictably.

This work contributes to the field of rehabilitation robotics by presenting a computationally efficient yet effective control method that can maintain system stability and precision, even under uncertain conditions. Future studies could further enhance this approach by incorporating adaptive control algorithms that continuously learn and adjust to individual patient characteristics during therapy. Additionally, integrating this con-

trol strategy with real-time feedback systems or machine learning models could further personalize neurorehabilitation and improve patient outcomes.

In conclusion, the proposed control framework offers a practical and robust solution for exoskeleton-based rehabilitation, overcoming the limitations of traditional computed torque controllers. By optimizing for both performance and computational load, this study lays a foundation for future advancements in neurorehabilitation technologies, promoting safer and more effective therapies.

8. Conclusions

In conclusion, this study presents a novel model reference computed torque controller designed to enhance the performance and stability of exoskeleton robots in neurorehabilitation. By addressing the limitations of traditional computed torque control, particularly its sensitivity to model inaccuracies, the proposed controller effectively manages parametric uncertainties while optimizing computational efficiency. The dynamic model of a seven-degrees-of-freedom lower limb exoskeleton, including realistic joint friction, ensures accurate representation of the robot's physical behavior. The dual-loop control system, combining a predictive slower loop and a corrective PID loop, enables precise trajectory tracking with reduced computational overhead. Excluding Coriolis and centrifugal forces from the model further streamlines processing without compromising the accuracy. The experimental results validate the system's robustness and confirm its potential for delivering reliable physical therapy and continuous recovery monitoring. This innovative approach offers significant improvements in control precision, paving the way for more effective and stable exoskeleton-assisted neurorehabilitation.

Funding: This research is supported by the Mechanical and Manufacturing Engineering Department, College of Engineering and Computing.

Data Availability Statement: Data are contained within the article.

Conflicts of Interest: The authors declare no conflict of interest.

References

1. Kyoungchul, K.; Doyoung, J. Design and control of an exoskeleton for the elderly and patients. *IEEE/ASME Trans. Mechatron.* **2006**, *11*, 428–432. [CrossRef]
2. Kong, K.; Moon, H.; Hwang, B.; Jeon, D.; Tomizuka, M. Impedance Compensation of SUBAR for Back-Drivable Force-Mode Actuation. *IEEE Trans. Robot.* **2009**, *25*, 512–521. [CrossRef]
3. Colombo, G.; Joerg, M.; Schreier, R.; Dietz, V. Treadmill training of paraplegic patients using a robotic orthosis. *J. Rehabil. Res. Dev.* **2000**, *37*, 693–700. [PubMed]
4. Bernhardt, M.; Frey, M.; Colombo, G.; Riener, R. Hybrid force-position control yields cooperative behaviour of the rehabilitation robot LOKOMAT. In Proceedings of the 9th International Conference on Rehabilitation Robotics, Chicago, IL, USA, 28 June 1–July 2005; ICORR 2005. pp. 536–539.
5. Veneman, J.F.; Kruidhof, R.; Hekman, E.E.G.; Ekkelenkamp, R.; Asseldonk, E.H.F.V.; Kooij, H.V.D. Design and Evaluation of the LOPES Exoskeleton Robot for Interactive Gait Rehabilitation. *IEEE Trans. Neural Syst. Rehabil. Eng.* **2007**, *15*, 379–386. [CrossRef] [PubMed]
6. Veneman, J.F.; Ekkelenkamp, R.; Kruidhof, R.; Helm, F.C.T.V.D.; Kooij, H.V.D. Design of a series elastic- and Bowden cable-based actuation system for use as torque-actuator in exoskeleton-type training. In Proceedings of the 9th International Conference on Rehabilitation Robotics, Chicago, IL, USA, 28 June 1–July 2005; ICORR 2005. pp. 496–499.
7. Banala, S.K.; Agrawal, S.K.; Scholz, J.P. Active Leg Exoskeleton (ALEX) for Gait Rehabilitation of Motor-Impaired Patients. In Proceedings of the 2007 IEEE 10th International Conference on Rehabilitation Robotics, Noordwijk, The Netherlands, 13–15 June 2007; pp. 401–407.
8. Agrawal, S.K.; Banala, S.K.; Fattah, A.; Sangwan, V.; Krishnamoorthy, V.; Scholz, J.P.; Hsu, W.-L. Assessment of Motion of a Swing Leg and Gait Rehabilitation with a Gravity Balancing Exoskeleton. *IEEE Trans. Neural Syst. Rehabil. Eng.* **2007**, *15*, 410–420. [CrossRef] [PubMed]
9. Kim, S.H.; Banala, S.K.; Brackbill, E.A.; Agrawal, S.K.; Krishnamoorthy, V.; Scholz, J.P. Robot-assisted modifications of gait in healthy individuals. *Exp. Brain Res.* **2010**, *202*, 809–824. [CrossRef] [PubMed]
10. Stegall, P.; Winfree, K.N.; Agrawal, S.K. Degrees-of-freedom of a robotic exoskeleton and human adaptation to new gait templates. In Proceedings of the 2012 IEEE International Conference on Robotics and Automation, Saint Paul, MN, USA, 14–18 May 2012; pp. 4986–4991.

11. Kawamoto, H.; Sankai, Y. Power assist method based on phase sequence driven by interaction between human and robot suit. In Proceedings of the RO-MAN 2004 13th IEEE International Workshop on Robot and Human Interactive Communication (IEEE Catalog No.04TH8759), Kurashiki, Japan, 22 September 2004; pp. 491–496.
12. Suzuki, K.; Mito, G.; Kawamoto, H.; Hasegawa, Y.; Sankai, Y. Intention-based walking support for paraplegia patients with Robot Suit HAL. *Adv. Robot.* **2007**, *21*, 1441–1469. [CrossRef]
13. Kawamoto, H.; Hayashi, T.; Sakurai, T.; Eguchi, K.; Sankai, Y. Development of single leg version of HAL for hemiplegia. In Proceedings of the 2009 Annual International Conference of the IEEE Engineering in Medicine and Biology Society, Minneapolis, MN, USA, 3–6 September 2009; pp. 5038–5043.
14. Zeilig, G.; Weingarden, H.; Zwecker, M.; Dudkiewicz, I.; Bloch, A.; Esquenazi, A. Safety and tolerance of the ReWalk exoskeleton suit for ambulation by people with complete spinal cord injury: A pilot study. *J. Spinal Cord. Med.* **2012**, *35*, 96–101. [CrossRef] [PubMed]
15. Esquenazi, A.; Talaty, M.; Packel, A.; Saulino, M. The ReWalk Powered Exoskeleton to Restore Ambulatory Function to Individuals with Thoracic-Level Motor-Complete Spinal Cord Injury. *Am. J. Phys. Med. Rehabil.* **2012**, *91*, 911–921. [CrossRef] [PubMed]
16. Shi, D.; Zhang, W.; Zhang, W.; Ding, X. A Review on Lower Limb Rehabilitation Exoskeleton Robots. *Chin. J. Mech. Eng.* **2019**, *32*, 74. [CrossRef]
17. Strickland, E. Good-bye, Wheelchair, Hello Exoskeleton. 2011. Available online: http://spectrum.ieee.org/biomedical/bionics/goodbye-wheelchair-hello-exoskeleton (accessed on 13 December 2020).
18. Farris, R.J.; Quintero, H.A.; Murray, S.A.; Ha, K.H.; Hartigan, C.; Goldfarb, M. A Preliminary Assessment of Legged Mobility Provided by a Lower Limb Exoskeleton for Persons with Paraplegia. *IEEE Trans. Neural Syst. Rehabil. Eng.* **2014**, *22*, 482–490. [CrossRef] [PubMed]
19. Sanz-Merodio, D.; Cestari, M.; Arevalo, J.C.; Garcia, E. Control Motion Approach of a Lower Limb Orthosis to Reduce Energy Consumption. *Int. J. Adv. Robot. Syst.* **2012**, *9*, 232. [CrossRef]
20. Neuhaus, P.D.; Noorden, J.H.; Craig, T.J.; Torres, T.; Kirschbaum, J.; Pratt, J.E. Design and evaluation of Mina: A robotic orthosis for paraplegics. In Proceedings of the 2011 IEEE International Conference on Rehabilitation Robotics, Zurich, Switzerland, 29 June 2011–1 July 2011; pp. 1–8.
21. Wang, L.; Wang, S.; Asseldonk, E.H.F.V.; Kooij, H.V.D. Actively controlled lateral gait assistance in a lower limb exoskeleton. In Proceedings of the 2013 IEEE/RSJ International Conference on Intelligent Robots and Systems, Tokyo, Japan, 3–7 November 2013; pp. 965–970.
22. Kim, J.-H.; Han, J.W.; Kim, D.Y.; Baek, Y.S. Design of a Walking Assistance Lower Limb Exoskeleton for Paraplegic Patients and Hardware Validation Using CoP. *Int. J. Adv. Robot. Syst.* **2013**, *10*, 113. [CrossRef]
23. Kai, K.H.; Noorden, J.H.; Missel, M.; Craig, T.; Pratt, J.E.; Neuhaus, P.D. Development of the IHMC Mobility Assist Exoskeleton. In Proceedings of the 2009 IEEE International Conference on Robotics and Automation, Kobe, Japan, 12–17 May 2009; pp. 2556–2562.
24. Tagliamonte, N.L.; Sergi, F.; Carpino, G.; Accoto, D.; Guglielmelli, E. Human-robot interaction tests on a novel robot for gait assistance. In Proceedings of the 2013 IEEE 13th International Conference on Rehabilitation Robotics (ICORR), Seattle, WA, USA, 24–26 June 2013; pp. 1–6.
25. Mori, Y.; Okada, J.; Takayama, K. Development of a standing style transfer system "ABLE" for disabled lower limbs. *IEEE/ASME Trans. Mechatron.* **2006**, *11*, 372–380. [CrossRef]
26. Yoshimitsu, T.; Yamamoto, K. Development of a power assist suit for nursing work. In Proceedings of the SICE 2004 Annual Conference, Sapporo, Japan, 4–6 August 2004; Volume 1, pp. 577–580.
27. Yamamoto, K.; Ishii, M.; Noborisaka, H.; Hyodo, K. Stand alone wearable power assisting suit—Sensing and control systems. In Proceedings of the RO-MAN 2004. 13th IEEE International Workshop on Robot and Human Interactive Communication (IEEE Catalog No.04TH8759), Okayama, Japan, 22 September 2004; pp. 661–666.
28. Zoss, A.B.; Kazerooni, H.; Chu, A. Biomechanical design of the Berkeley lower extremity exoskeleton (BLEEX). *IEEE/ASME Trans. Mechatron.* **2006**, *11*, 128–138. [CrossRef]
29. Kazerooni, H.; Steger, R.; Huang, L. Hybrid Control of the Berkeley Lower Extremity Exoskeleton (BLEEX). *Int. J. Robot. Res.* **2006**, *25*, 561–573. [CrossRef]
30. Chen, B.; Zhong, C.-H.; Zhao, X.; Ma, H.; Guan, X.; Li, X.; Liang, F.-Y.; Cheng, J.C.Y.; Qin, L.; Law, S.-W.; et al. A wearable exoskeleton suit for motion assistance to paralysed patients. *J. Orthop. Transl.* **2017**, *11*, 7–18. [CrossRef] [PubMed]
31. Chen, B.; Zhong, C.; Zhao, X.; Ma, H.; Qin, L.; Liao, W. Reference Joint Trajectories Generation of CUHK-EXO Exoskeleton for System Balance in Walking Assistance. *IEEE Access* **2019**, *7*, 33809–33821. [CrossRef]
32. Hyon, S.; Morimoto, J.; Matsubara, T.; Noda, T.; Kawato, M. XoR: Hybrid drive exoskeleton robot that can balance. In Proceedings of the 2011 IEEE/RSJ International Conference on Intelligent Robots and Systems, San Francisco, CA, USA, 25–30 September 2011; pp. 3975–3981.
33. Nguyen-Tuong, D.; Peters, J. Learning Robot Dynamics for Computed Torque Control Using Local Gaussian Processes Regression. In Proceedings of the 2008 ECSIS Symposium on Learning and Adaptive Behaviors for Robotic Systems (LAB-RS), Edinburgh, UK, 6–8 August 2008; pp. 59–64.
34. Kurz, T. Normal Ranges of Joint Motion. 2015. Available online: http://web.mit.edu/tkd/stretch/stretching_8.html (accessed on 23 September 2024).

35. American Academy of Orthopaedic Surgeons. *Joint Motion: Methods of Measuring and Recording*; American Academy of Orthopaedic Surgeons: Chicago, IL, USA.
36. Kendall, F.P.; McCreary, E.K.; Provance, P.G.; Rodgers, M.M.; Romani, W.A. *Muscles: Testing and Function, with Posture and Pain*, 5th ed.; LWW: Philadelphia, PN, USA, 2005.
37. Nikolova, G.; Toshev, Y. Comparison of two approaches for calculation of the geometric and inertial characteristics of the human body of the Bulgarian population. *Acta Bioeng. Biomech.* **2008**, *10*, 3–8.
38. Craig, J.J. *Introduction to Robotics: Mechanics and Control*; Pearson/Prentice Hall: Upper Saddle River, NJ, USA, 2005.
39. Liu, S.; Chen, G.S. *Dynamics and Control of Robotic Manipulators with Contact and Friction. 2018*; John Wiley & Sons: Hoboken, NJ, USA.
40. Pennestrì, E.; Rossi, V.; Salvini, P.; Valentini, P.P. Review and comparison of dry friction force models. *Nonlinear Dyn.* **2016**, *83*, 1785–1801. [CrossRef]
41. Ha, J.-L.; Fung, R.-F.; Han, C.-F.; Chang, J.-R. Effects of Frictional Models on the Dynamic Response of the Impact Drive Mechanism. *J. Vib. Acoust.* **2005**, *128*, 88–96. [CrossRef]
42. Hasan, S.K.; Dhingra, A.K. Development of a model reference computed torque controller for a human lower extremity exoskeleton robot. *Proc. Inst. Mech. Eng. Part I J. Syst. Control. Eng.* **2021**, *235*, 1615–1637. [CrossRef]

Disclaimer/Publisher's Note: The statements, opinions and data contained in all publications are solely those of the individual author(s) and contributor(s) and not of MDPI and/or the editor(s). MDPI and/or the editor(s) disclaim responsibility for any injury to people or property resulting from any ideas, methods, instructions or products referred to in the content.